The mean star formation rates of unobscured QSOs: searching for evidence of suppressed or enhanced star formation

F. Stanley,[1,2]★ D. M. Alexander,[2] C. M. Harrison,[2,3] D. J. Rosario,[2] L. Wang,[2,4,5] J. A. Aird,[6] N. Bourne,[7] L. Dunne,[7,8] S. Dye,[9] S. Eales,[8] K. K. Knudsen,[1] M. J. Michałowski,[7,10] E. Valiante,[8] G. De Zotti,[11] C. Furlanetto,[9,12] R. Ivison,[3,7] S. Maddox[7,8] and M. W. L. Smith[8]

[1]*Department of Space Earth and Environment, Chalmers University of Technology, Onsala Space Observatory, SE-43992 Onsala, Sweden*
[2]*Center for Extragalactic Astronomy, Department of Physics, Durham University, South Road, Durham DH1 3LE, UK*
[3]*European Southern Observatory, Karl-Schwarzschild-Str 2, D-85748 Garching b. München, Germany*
[4]*SRON Netherlands Institute for Space Research, Landleven 12, NL-9747 AD Groningen, the Netherlands*
[5]*Kapteyn Astronomical Institute, University of Groningen, Postbus 800, NL-9700 AV Groningen, the Netherlands*
[6]*Institute of Astronomy, University of Cambridge, Madingley Road, Cambridge CB3 0HA, UK*
[7]*SUPA (Scottish Universities Physics Alliance), Institute for Astronomy, University of Edinburgh, Royal Observatory Blackford Hill, Edinburgh EH9 3HJ, UK*
[8]*School of Physics and Astronomy, Cardiff University, Queen's Buildings, Cardiff CF24 3AA, UK*
[9]*School of Physics and Astronomy, University of Nottingham, University Park, Nottingham NG7 2RD, UK*
[10]*Astronomical Observatory Institute, Faculty of Physics, Adam Mickiewicz University, ul. Słoneczna 36, PL-60-286 Poznań, Poland*
[11]*INAF – Osservatorio Astronomico di Padova, Vicolo dell'Osservatorio 5, I-35122 Padova, Italy*
[12]*CAPES Foundation, Ministry of Education of Brazil, 70040-020 Brasília, DF, Brazil*

ABSTRACT

We investigate the mean star formation rates (SFRs) in the host galaxies of ∼3000 optically selected quasi-stellar objects (QSOs) from the Sloan Digital Sky Survey within the *Herschel*-ATLAS fields, and a radio-luminous subsample covering the redshift range of $z = 0.2$–2.5. Using *Wide-field Infrared Survey Explorer (WISE)* and *Herschel* photometry (12–500 μm) we construct composite spectral energy distributions (SEDs) in bins of redshift and active galactic nucleus (AGN) luminosity. We perform SED fitting to measure the mean infrared luminosity due to star formation, removing the contamination from AGN emission. We find that the mean SFRs show a weak positive trend with increasing AGN luminosity. However, we demonstrate that the observed trend could be due to an increase in black hole (BH) mass (and a consequent increase of inferred stellar mass) with increasing AGN luminosity. We compare to a sample of X-ray selected AGN and find that the two populations have consistent mean SFRs when matched in AGN luminosity and redshift. On the basis of the available virial BH masses, and the evolving BH mass to stellar mass relationship, we find that the mean SFRs of our QSO sample are consistent with those of main sequence star-forming galaxies. Similarly the radio-luminous QSOs have mean SFRs that are consistent with both the overall QSO sample and with star-forming galaxies on the main sequence. In conclusion, on average QSOs reside on the main sequence of star-forming galaxies, and the observed positive trend between the mean SFRs and AGN luminosity can be attributed to BH mass and redshift dependencies.

Key words: galaxies: active – galaxies: evolution – quasars: general – galaxies: star formation.

1 INTRODUCTION

The co-evolution of a galaxy and its central supermassive black hole (BH) is a case argued by both empirical observations (e.g. the correlation of the mass of the BH and the galaxy spheroid) and results from cosmological models of galaxy evolution (see Alexander & Hickox 2012; Fabian 2012; Kormendy & Ho 2013 for reviews). This co-evolution of the galaxy and the central BH could be a result of a connection between the processes of star formation and BH growth. The former is commonly quantified using the star formation rate (SFR), and the latter by the luminosity of the active galactic

nucleus (AGN; visible during episodes of BH growth). Since both processes are primarily fuelled by the cold gas supply within the galaxy, we may expect a first order connection between the two processes. However, models of galaxy evolution require a more interactive connection, with the AGN having a regulating role over the amount of available cold gas, and hence the SFR of the galaxy (e.g. Di Matteo, Springel & Hernquist 2005; Bower et al. 2006; Genel et al. 2014; Schaye et al. 2015).

To investigate if the AGN has indeed a regulatory role on the SFR of a galaxy there have been many studies on the star-forming properties of galaxies hosting AGN (see Harrison 2017 review). With observations from the *Herschel Space Observatory* (*Herschel*; Pilbratt et al. 2010) we can place strong constraints on the far-infrared (FIR) emission of galaxies (λ = 30–500 μm), which traces the reprocessed emission from the dusty star-forming regions (see Casey, Narayanan & Cooray 2014; Lutz 2014). Combining *Herschel* FIR observations with deep X-ray or optical observations, it is possible to independently constrain the AGN power in the X-ray and optical, while placing strong constraints on the SFR of the host in the FIR. However, since it is also possible for the AGN to contribute to the FIR luminosity due to the thermal re-radiation of obscuring dust from the surrounding torus (e.g. Antonucci 1993), it is important to decompose the AGN and star-formation emission at infrared wavelengths (e.g. Netzer et al. 2007; Mullaney et al. 2011; Del Moro et al. 2013; Delvecchio et al. 2014).

The majority of FIR studies of X-ray selected AGN that reach moderate to high AGN luminosities ($L_{\rm AGN,bol} < 10^{45-46}$ erg s^{-1}) find that the mean SFRs as a function of AGN luminosity show flat trends independently of redshift, up to $z \sim 3$ (e.g. Harrison et al. 2012; Mullaney et al. 2012; Rosario et al. 2012; Azadi et al. 2015; Stanley et al. 2015; Lanzuisi et al. 2017). Although this is in discrepancy with some earlier studies reporting negative trends between the mean SFRs and AGN luminosity (e.g. Page et al. 2012), an analysis by Harrison et al. (2012) demonstrated how these results are driven by small number statistics. Indeed, following studies (e.g. Azadi et al. 2015; Stanley et al. 2015; Lanzuisi et al. 2017) that used large samples of X-ray selected AGN all converge to the same results of a flat trend between the mean SFRs and AGN luminosity. In Stanley et al. (2015) we demonstrated how the flat trends can be reproduced by empirical 'toy models' that assume AGN live in star-forming galaxies (Aird et al. 2013; Hickox et al. 2014), but with AGN activity as a stochastic process, with the probability of an AGN at a given luminosity defined by the observed Eddington ratio distribution (e.g. Aird et al. 2012).

Recently hydrodynamical simulations of both isolated mergers and of full cosmological volumes have also been able to reproduce the observed flat trend between the average SFR and AGN luminosity for populations of galaxies hosting low to moderate AGN luminosities (i.e. $L_{\rm AGN,bol} < 10^{45}$ erg s^{-1}; e.g. Volonteri et al. 2015; McAlpine et al. 2017). In agreement with the simple 'toy models', these simulations find that AGN luminosities can vary over several orders of magnitude for a fixed SFR (or stellar mass). However, in the simulations the underlying connection between these two processes is non-universal and can be sensitive to different feeding and feedback prescriptions invoked by the simulations (e.g. Thacker et al. 2014). Crucial tests of these simulations will be to correctly reproduce the SFRs for the galaxies that host the most luminous AGN, such as quasi-stellar objects (QSOs), luminous in the optical (with $L_{\rm AGN,bol} > 10^{45}$ erg s^{-1}) and/or very luminous in the radio (roughly $L_{\rm 1.4GHz} \gtrsim 10^{24}$ W Hz^{-1}). Such AGN have the most

energetic outputs, and may be the most likely to impact directly upon the star formation of their host galaxies (e.g. Bower et al. 2017).

FIR studies of optically selected QSOs at $z \gtrsim 0.2$ are finding that they tend to live in galaxies with ongoing star formation (e.g. Kalfountzou et al. 2014; Gürkan et al. 2015; Harris et al. 2016; Netzer et al. 2016) at levels consistent with those of the star-forming population (e.g. Rosario et al. 2013). When looking at the mean SFR as a function of the bolometric AGN luminosity some studies argue for a positive correlation (e.g. Bonfield et al. 2011; Rosario et al. 2013; Kalfountzou et al. 2014; Gürkan et al. 2015; Harris et al. 2016). However, when the QSOs are selected to be FIR luminous, the mean SFR shows a flat trend with the bolometric AGN luminosity (e.g. Pitchford et al. 2016).

The most powerful AGN can sometimes also be traced by their radio emission. Powerful radio AGN can be selected in multiple ways such as a simple radio luminosity cut (e.g. McAlpine, Jarvis & Bonfield 2013; Magliocchetti et al. 2014), based on their radio loudness (i.e. ratio of radio to optical luminosity; $R_i = L(5\,{\rm GHz})/L(4000\,{\rm \AA})$; Kellermann et al. 1989), which is used to split between radio-loud ($R_i > 10$) and radio-quiet AGN, or based on their excitation level (or radiative efficiency), between low-excitation (radiatively inefficient) and high-excitation (radiatively efficient) radio galaxies (LERGs and HERGs, respectively; Best & Heckman 2012 and references therein). FIR studies of radio AGN, with samples of HERG-type AGN, find that at $z \gtrsim 0.2$ their hosts have ongoing star formation, independent of selection methods (e.g. Seymour et al. 2011; Drouart et al. 2014, 2016; Kalfountzou et al. 2014; Karouzos et al. 2014; Magliocchetti et al. 2014; Gürkan et al. 2015; Podigachoski et al. 2016). Studies taking a luminosity cut where only the most luminous radio AGN are selected find evidence of intense FIR emission and star formation, at similar levels to the radio selected star-forming galaxies, at redshifts of $z \gtrsim 1$ (e.g. Magliocchetti et al. 2014, 2016). Studies selecting radio-loud AGN are showing evidence of a positive trend of mean SFRs with both radio AGN luminosity (e.g. Karouzos et al. 2014), optically derived AGN bolometric luminosity (e.g. Kalfountzou et al. 2014; Gürkan et al. 2015) and AGN torus luminosity (e.g. Podigachoski et al. 2016). However, it is worth noting that LERG-type AGN tend to show lower SFRs than HERG-type AGN (e.g. Hardcastle et al. 2013; Gürkan et al. 2015).

A key limitation in the majority of previous studies is that they have not simultaneously taken into account the observed stellar mass and redshift dependencies of SFR observed for the global galaxy population. The average global SFR of galaxies increases with increasing redshift up to $z \sim 2$–3 where we observe the peak of cosmic star formation. The increase of the typical SFR with redshift has also been established for QSO samples, through studying the SFR volume density (e.g. Serjeant et al. 2010) and through the use of maximum likelihood estimators to establish a correlation (e.g. Bonfield et al. 2011). Furthermore, there is a well-known stellar mass dependency of the SFR, for actively star-forming systems, which is called the main sequence of star-forming galaxies (e.g. Elbaz et al. 2007; Noeske et al. 2007; Whitaker et al. 2012; Schreiber et al. 2015). Indeed, some studies found that the BH mass (and the inferred stellar mass) is an important factor when studying the SFRs of QSOs (e.g. Rosario et al. 2013; Harris et al. 2016). These effects could be driving the observed correlations of the SFR with AGN luminosity, and need to be simultaneously taken into account when investigating such trends. An additional source of uncertainty in some studies on the SFRs of galaxies hosting AGN is the fact that observed powerful AGN could be contributing significantly to the
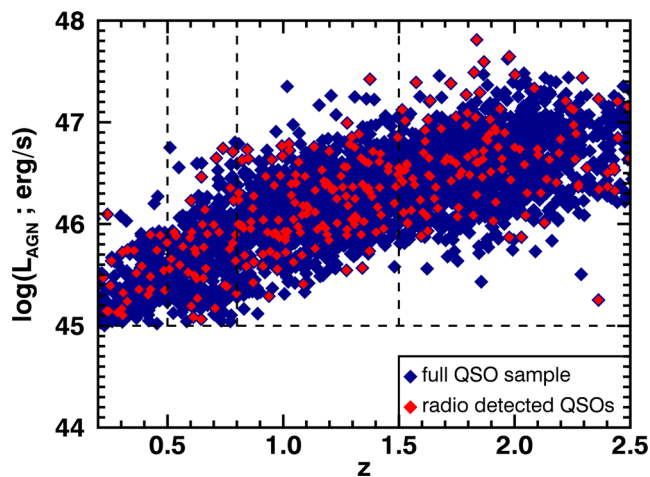
Figure 1. AGN bolometric luminosity ($L_{AGN,bol}$) versus redshift (z) for the full QSO sample from SDSS DR7 covered by H-ATLAS in the NGP, GAMA9, GAMA12 and GAMA15 fields. The vertical dashed lines indicate the redshift ranges taken in our analysis, and the horizontal dashed line shows the $L_{AGN,bol}$ cut that defines the sample (see Section 2.1). In red we highlight the radio detected sources from the FIRST radio catalogue (see Section 2.3). Within the redshift range of interest ($z = 0.2$–2.5) there are a total of 3026 optically selected QSOs.

FIR luminosities (e.g. Drouart et al. 2014; Symeonidis et al. 2016). Not removing the potential AGN contamination to the FIR photometry used to derive SFRs can cause an artificial boost in the SFR values.

In this work, we aim to overcome the limitations outlined above. We define the mean SFRs of more than 3000 optical QSOs, selected based on their broad optical emission lines, at $10^{45} < L_{AGN,bol} < 10^{48}$ erg s^{-1}, and a subsample of 258 radio-luminous QSOs of $L_{1.4\,GHz} > 10^{24}$ W Hz^{-1}, over the redshift range of $0.2 < z < 2.5$. Although not selected based on the excitation level criteria, our sample consists of HERG-type AGN. We compare our results to the normal star-forming galaxies of the same epoch, expanding the work of Rosario et al. (2013) to higher $L_{AGN,bol}$ and lower redshifts. Furthermore, we expand the $\langle SFR \rangle - L_{AGN,bol}$ plane of Stanley et al. (2015) to higher AGN luminosities. In our analysis we will simultaneously take into account of both redshift and stellar mass dependencies, and remove AGN contamination from the IR luminosity. The paper is organized as follows. In Section 2 we define the sample and photometry used in our work. In Section 3 we present the methods followed, and in Section 4 we present our initial results. Finally, in Section 5 we discuss our methods and the results of our analysis, and in Section 6 we present the conclusions of this work. Throughout this paper we assume $H_0 = 70$ km s^{-1} Mpc^{-1}, $\Omega_M = 0.3$, $\Omega_\Lambda = 0.7$ and a Chabrier (2003) initial mass function (IMF), unless otherwise specified.

2 SAMPLE AND DATA USED

The aim of this work is to constrain the mean SFRs as a function of AGN bolometric luminosity, out to very high AGN luminosities ($L_{AGN,bol} \sim 10^{48}$ erg s^{-1}; see Fig. 1), in addition to investigating dependencies of the mean SFRs on the presence of a radio-luminous AGN.

FIR photometry provides one of the best measures of the SFR, as it traces the peak of the dust-reprocessed emission from star-forming regions (e.g. Kennicutt 1998; Calzetti et al. 2010; Domínguez Sánchez et al. 2014; Rosario et al. 2016). Furthermore, when study-

ing QSO samples the optical–ultraviolet (UV) is no longer an option for determining the star formation as the QSO light dominates at these wavelengths. We use FIR data from the *Herschel*-ATLAS (H-ATLAS) observational program (Eales et al. 2010; Section 2.2) that covered the fields of GAMA09, GAMA12 and GAMA15 in its Phase 1, and the North and South Galactic Pole (NGP and SGP, respectively) in its Phase 2 observations. The H-ATLAS fields benefit from multiwavelength coverage (see Bourne et al. 2016 for a detailed description of all accompanying data), with excellent optical [Sloan Digital Sky Survey (SDSS); Section 2.1], mid-infrared (MIR) and FIR photometry [*Wide-field Infrared Survey Explorer* (*WISE*) and *Herschel*; Section 2.2], and radio observations [Faint Images of the Radio Sky at Twenty cm (FIRST); Section 2.3]. We use the available data to draw a sample of optically selected QSOs from the SDSS with *WISE* and *Herschel* coverage (see Section 2.1), determine a radio-luminous subsample of QSOs using the FIRST survey (see Section 2.3) and measure their SFRs using *WISE* and *Herschel* observations. As we only study the fields that have overlap with the SDSS area, we exclude the SGP field.

2.1 Optical/SDSS QSOs

To define our QSO sample we use the publicly available SDSS Data Release 7 (DR7) QSO catalogue as presented in Shen et al. (2011) (see also Schneider et al. 2010 for original selection of QSOs). We chose this release as it includes the spectral analysis and virial BH mass estimates.

To provide a measurement of the power of the QSOs we use the AGN bolometric luminosity ($L_{AGN,bol}$) as given in Shen et al. (2011), which has been derived from $L_{5100\,Å}$, $L_{3000\,Å}$ and $L_{1350\,Å}$ for sources at redshifts of $z < 0.7$, $0.7 \leq z < 1.9$ and $z \geq 1.9$, respectively, using the spectral fits and bolometric corrections from the composite SED in Richards et al. (2006) (BC$_{5100\,Å} = 9.26$, BC$_{3000\,Å} = 5.15$ and BC$_{1350\,Å} = 3.81$; see Shen et al. 2011). All the QSOs of our sample have bolometric luminosities of $L_{AGN,bol} \gtrsim 10^{45}$ erg s^{-1} (see Fig. 1). We constrain the sample of QSOs within the regions covered by H-ATLAS.

We also make use of the virial BH mass (M_{BH}) estimates from Shen et al. (2011), from which we estimate the stellar masses (see Section 5.2.1 and equation 4). The M_{BH} have been calculated using the full width at half-maximum (FWHM) and continuum luminosities of the Hβ, Mg II and C IV lines (see section 3 of Shen et al. 2011). Specifically, the M_{BH} is estimated from Hβ for sources with redshifts of $z < 0.7$, from Mg II for sources with $0.7 < z \leq 1.9$ and from C IV for sources with $z > 1.9$. In Fig. 2 we show the M_{BH} values of our sample as a function of $L_{AGN,bol}$. For comparison we also indicate three different levels of the Eddington ratio, λ_{edd}, the ratio of $L_{AGN,bol}$ over the Eddington luminosity. The λ_{edd} of our sample covers a dynamic range of three orders of magnitude, with a mean and median value of 0.34 and 0.24, respectively.

Overall, this study looks at sources with redshifts of $z = 0.2$–2.5, and includes a total of 3026 QSOs with BH masses and AGN bolometric luminosities of predominantly $10^7 < M_{BH} < 10^{10}$ M$_\odot$ and $10^{45} < L_{AGN,bol} < 3 \times 10^{47}$ erg s^{-1}, respectively.

2.2 Mid-infrared and far-infrared photometry

For our analysis we stack the matched-filter-smoothed Photodetector Array Camera and Spectrometer (PACS) and Spectral and Photometric Imaging REceiver (SPIRE) image products provided by the H-ATLAS team (see Valiante et al. 2016) for the four fields of GAMA09 (54 deg^2), GAMA12 (54 deg^2), GAMA15 (54 deg^2)
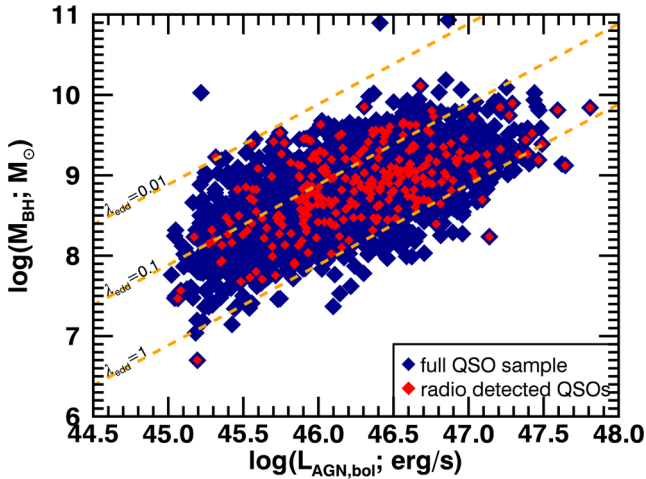
Figure 2. The BH mass (M_{BH}) as a function of AGN bolometric luminosity ($L_{AGN,bol}$) for the full QSO sample (see Section 2). The yellow dashed lines correspond to constant Eddington ratios (λ_{Edd} of 0.01, 0.1 and 1), for comparison.

and NGP (150 deg^2) that overlap with the SDSS. Detailed information on the construction of the images is presented in Valiante et al. (2016). The images used in our analysis have had the large-scale background subtracted (i.e. the cirrus emission within our Galaxy), and each pixel contains the best estimate of the flux density of a point source at that position, making them ideal for stacking analyses. In addition to the images there are also noise maps available that provide the instrumental noise at each pixel.

To define the MIR properties of our sample we use the *WISE* all-sky survey (Wright et al. 2010).[1] Using a radius of 1 arcsec we match to the optical positions of our QSO sample described in Section 2.1, with a spurious match fraction of ∼0.1 per cent.[2] We find that 94.2 per cent of our sources have a *WISE* counterpart. Sources in the catalogue with less than a 2σ significance at a given band have been attributed an upper limit defined by the integrated flux density measurement plus two times the measurement uncertainty. In the cases were the flux density is negative then the upper limit is defined as two times the measurement uncertainty (see the explanatory supplement to the *WISE* All-Sky Data Release, accessible through the link given in Footnote 1). For our SED fitting analysis (Section 3.3) we use the W3 and W4 bands at 12 and 22 μm, respectively.

---

[1] The *WISE* all-sky catalogue is available at: http://irsa.ipac.caltech.edu/Missions/wise.html

[2] To choose the matching radius and estimate the spurious match fraction, we follow the procedure outlined below. First we take all matches between the two catalogues that are within 20 arcsec, and produce the distribution of the number of matches in bins of increasing separation. The shape of the distribution has a characteristic shape, with a peak around 0 arcsec separation, followed by a fairly steep decrease until it reaches a minimum in the number of matches. Once the separation passes the point of minimum matches, there is a steady increase in the number of matches as the separation increases. We chose the matching radius to be the separation where the minimum in the distribution occurs, and use the slope of increasing number of matches at the large separation end of the distribution to extrapolate to the smaller separations and estimate the number of spurious matches within the chosen matching radius.
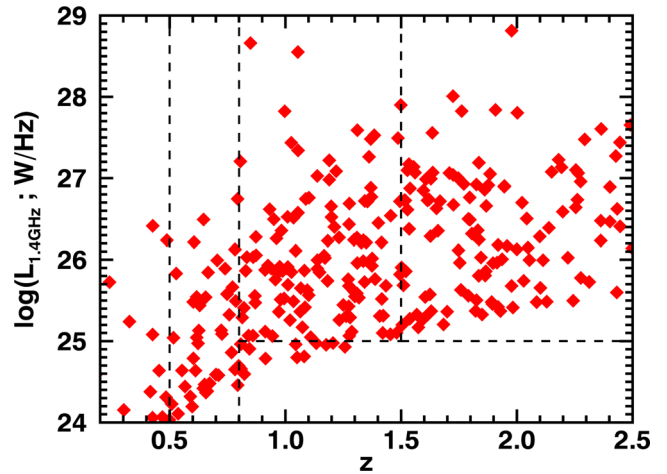

Figure 3. Radio luminosity from the FIRST survey ($L_{1.4\,GHz}$) versus redshift (z), for the radio detected QSOs in our sample. The vertical dashed lines indicate the redshift ranges taken in our analysis, and the horizontal dashed lines show the $L_{1.4\,GHz}$ limits used to define sources as radio-luminous. A total of 258 are classified as radio-luminous within the redshift range of interest ($z = 0.2$–2.5; see Section 2.3).

2.3 Radio data and classification

To determine the radio luminosities of our QSO sample we use the FIRST radio catalogue (Becker, White & Helfand 1995), which covers the full sky area observed by SDSS, to a sensitivity of 1 mJy. To identify the radio detected QSOs we matched the SDSS QSO catalogue to the FIRST catalogue using a 2 arcsec radius, to minimize the number of spurious matches, with a resulting spurious match fraction of ∼1.4 per cent (see Footnote 2). We calculate the 1.4 GHz luminosity ($L_{1.4\,GHz}$) from the catalogued flux densities, using the following equation:

$$L_{1.4\,GHz} = 4\pi D^2 F_{1.4\,GHz}(1+z)^{-(1-\alpha)}, \tag{1}$$

where D is the luminosity distance, $F_{1.4\,GHz}$ is the catalogued flux density and assuming $f_\nu \propto \nu^{-\alpha}$ with a spectral index of $\alpha = 0.8$. In Fig. 3 we plot the radio luminosity of the radio detected sources as a function of redshift.

We classify sources as radio-luminous AGN, using a luminosity lower limit cut of $L_{1.4\,GHz} > 10^{24}$ W Hz^{-1} for $z < 0.8$, and $L_{1.4\,GHz} > 10^{25}$ W Hz^{-1} for $z > 0.8$ (see Fig. 3). Based on work from McAlpine et al. (2013), Magliocchetti et al. (2016) argue that the radio luminosity beyond which the contribution by star-forming galaxies to the total radio luminosity function becomes negligible, increases from $10^{22.8}$ W Hz^{-1} in the local Universe up to $L_{1.4\,GHz,limit} = 10^{24.6}$ W Hz^{-1} at redshift of $z \sim 1.8$, after which it remains constant. Our luminosity cut is always higher than these thresholds, indicating that we are selecting sources where the AGN is dominating the radio emission, and do not expect star-forming galaxies to be contaminating our selection. Furthermore, in Section 4.3 we demonstrate how the radio luminosities of this sample are >1–3 orders of magnitude higher than the radio luminosities predicted from the IR luminosities due to star formation. Therefore we are selecting only AGN-dominated radio sources. Within the redshift range studied here ($z = 0.2$–2.5), there are 258 QSOs classified as radio-luminous.

Table 1. The mean source properties for each z–$L_{AGN,bol}$ bin in our sample of optical QSOs. Column (1): the ID of the bin that corresponds to the SEDs presented in the appendix. Column (2): the number of sources in each bin. Column (3): the mean redshift of each bin. Column (4): the mean BH mass of each bin. Column (5): the mean AGN bolometric luminosity (derived from the optical) of each bin. The uncertainties in columns (3), (4) and (5) correspond to the 16th–84th percentiles of the values in each bin. Column (6): the mean IR luminosity due to star formation from the best-fitting SED of each bin, the uncertainties are defined by the combination of the error on the fit and the range of $\langle L_{IR,SF}\rangle$ values from the other star-forming templates (see Section 3.3).

ID	N	$\langle z\rangle$	$\langle M_{BH}\rangle$ ($M_\odot$)	$\langle L_{AGN,bol}\rangle$ (erg s^{-1})	$\langle L_{IR,SF}\rangle$ (erg s^{-1})
(1)	(2)	(3)	(4)	(5)	(6)
F1	83	$0.321^{+0.078}_{-0.075}$	$0.37^{+0.25}_{-0.30}\times10^9$	$0.14^{+0.03}_{-0.02}\times10^{46}$	$0.38^{+0.10}_{-0.03}\times10^{45}$
F2	80	$0.394^{+0.067}_{-0.076}$	$0.30^{+0.21}_{-0.23}\times10^9$	$0.23^{+0.04}_{-0.03}\times10^{46}$	$0.59^{+0.24}_{-0.05}\times10^{45}$
F3	88	$0.410^{+0.059}_{-0.054}$	$0.46^{+0.09}_{-0.36}\times10^9$	$0.50^{+0.16}_{-0.18}\times10^{46}$	$0.67^{+0.29}_{-0.06}\times10^{45}$
F4	94	$0.640^{+0.114}_{-0.102}$	$0.33^{+0.24}_{-0.25}\times10^9$	$0.22^{+0.07}_{-0.07}\times10^{46}$	$0.78^{+0.17}_{-0.15}\times10^{45}$
F5	89	$0.635^{+0.107}_{-0.082}$	$0.47^{+0.25}_{-0.36}\times10^9$	$0.42^{+0.07}_{-0.07}\times10^{46}$	$0.84^{+0.10}_{-0.10}\times10^{45}$
F6	94	$0.670^{+0.098}_{-0.089}$	$0.66^{+0.48}_{-0.47}\times10^9$	$0.66^{+0.13}_{-0.09}\times10^{46}$	$1.52^{+0.22}_{-0.22}\times10^{45}$
F7	96	$0.697^{+0.076}_{-0.066}$	$1.12^{+0.60}_{-0.84}\times10^9$	$1.64^{+0.74}_{-0.73}\times10^{46}$	$1.52^{+0.15}_{-0.13}\times10^{45}$
F8	85	$0.989^{+0.161}_{-0.156}$	$0.61^{+0.40}_{-0.46}\times10^9$	$0.36^{+0.10}_{-0.11}\times10^{46}$	$1.56^{+0.34}_{-0.36}\times10^{45}$
F9	86	$1.133^{+0.210}_{-0.189}$	$0.63^{+0.54}_{-0.42}\times10^9$	$0.63^{+0.10}_{-0.10}\times10^{46}$	$2.08^{+0.35}_{-0.89}\times10^{45}$
F10	89	$1.100^{+0.248}_{-0.236}$	$0.80^{+0.39}_{-0.55}\times10^9$	$0.88^{+0.07}_{-0.06}\times10^{46}$	$2.32^{+0.52}_{-0.46}\times10^{45}$
F11	90	$1.080^{+0.216}_{-0.181}$	$0.74^{+0.48}_{-0.43}\times10^9$	$1.08^{+0.08}_{-0.09}\times10^{46}$	$3.22^{+0.64}_{-0.73}\times10^{45}$
F12	86	$1.104^{+0.255}_{-0.202}$	$1.03^{+0.44}_{-0.65}\times10^9$	$1.30^{+0.08}_{-0.06}\times10^{46}$	$2.08^{+0.19}_{-0.19}\times10^{45}$
F13	82	$1.132^{+0.185}_{-0.166}$	$1.01^{+0.69}_{-0.64}\times10^9$	$1.49^{+0.07}_{-0.08}\times10^{46}$	$1.63^{+0.44}_{-0.31}\times10^{45}$
F14	84	$1.157^{+0.203}_{-0.191}$	$0.97^{+0.60}_{-0.60}\times10^9$	$1.70^{+0.07}_{-0.06}\times10^{46}$	$1.90^{+0.75}_{-0.76}\times10^{45}$
F15	82	$1.175^{+0.181}_{-0.202}$	$1.21^{+0.90}_{-0.79}\times10^9$	$1.92^{+0.07}_{-0.07}\times10^{46}$	$2.89^{+0.29}_{-0.29}\times10^{45}$
F16	89	$1.223^{+0.151}_{-0.140}$	$1.14^{+0.60}_{-0.65}\times10^9$	$2.16^{+0.09}_{-0.10}\times10^{46}$	$2.63^{+0.28}_{-0.28}\times10^{45}$
F17	87	$1.273^{+0.200}_{-0.173}$	$1.29^{+0.71}_{-0.79}\times10^9$	$2.46^{+0.10}_{-0.11}\times10^{46}$	$4.08^{+1.75}_{-0.55}\times10^{45}$
F18	85	$1.245^{+0.202}_{-0.204}$	$1.39^{+0.67}_{-0.76}\times10^9$	$2.93^{+0.18}_{-0.19}\times10^{46}$	$3.26^{+0.36}_{-1.36}\times10^{45}$
F19	87	$1.254^{+0.201}_{-0.187}$	$1.74^{+0.40}_{-0.87}\times10^9$	$3.63^{+0.40}_{-0.35}\times10^{46}$	$3.37^{+0.31}_{-0.30}\times10^{45}$
F20	99	$1.272^{+0.188}_{-0.229}$	$2.34^{+1.49}_{-1.37}\times10^9$	$7.05^{+2.42}_{-2.61}\times10^{46}$	$2.22^{+1.17}_{-0.25}\times10^{45}$
F21	86	$1.750^{+0.158}_{-0.205}$	$1.02^{+0.74}_{-0.72}\times10^9$	$0.93^{+0.21}_{-0.23}\times10^{46}$	$2.10^{+0.27}_{-0.27}\times10^{45}$
F22	90	$1.847^{+0.237}_{-0.236}$	$1.22^{+0.80}_{-0.86}\times10^9$	$1.46^{+0.18}_{-0.18}\times10^{46}$	$1.78^{+0.36}_{-0.36}\times10^{45}$
F23	93	$1.854^{+0.330}_{-0.299}$	$1.13^{+0.77}_{-0.80}\times10^9$	$1.94^{+0.18}_{-0.16}\times10^{46}$	$4.94^{+0.52}_{-0.52}\times10^{45}$
F24	88	$1.785^{+0.330}_{-0.240}$	$1.84^{+0.98}_{-1.25}\times10^9$	$2.36^{+0.12}_{-0.11}\times10^{46}$	$4.00^{+1.51}_{-0.51}\times10^{45}$
F25	91	$1.777^{+0.233}_{-0.217}$	$1.69^{+1.39}_{-1.12}\times10^9$	$2.76^{+0.14}_{-0.14}\times10^{46}$	$3.36^{+1.38}_{-1.43}\times10^{45}$
F26	97	$1.782^{+0.254}_{-0.216}$	$1.59^{+1.04}_{-1.02}\times10^9$	$3.21^{+0.18}_{-0.17}\times10^{46}$	$4.04^{+1.54}_{-1.58}\times10^{45}$
F27	90	$1.776^{+0.209}_{-0.217}$	$1.63^{+0.98}_{-1.04}\times10^9$	$3.65^{+0.13}_{-0.13}\times10^{46}$	$2.67^{+1.17}_{-1.00}\times10^{45}$
F28	93	$1.853^{+0.207}_{-0.251}$	$1.97^{+1.29}_{-1.34}\times10^9$	$4.12^{+0.18}_{-0.19}\times10^{46}$	$1.81^{+0.32}_{-0.32}\times10^{45}$
F29	88	$1.859^{+0.256}_{-0.262}$	$2.16^{+1.30}_{-1.49}\times10^9$	$4.64^{+0.26}_{-0.21}\times10^{46}$	$3.80^{+1.67}_{-1.53}\times10^{45}$
F30	80	$1.879^{+0.224}_{-0.257}$	$2.12^{+1.33}_{-1.21}\times10^9$	$5.42^{+0.29}_{-0.29}\times10^{46}$	$5.19^{+1.43}_{-1.19}\times10^{45}$
F31	93	$1.911^{+0.240}_{-0.244}$	$2.30^{+0.78}_{-1.22}\times10^9$	$6.40^{+0.43}_{-0.35}\times10^{46}$	$6.85^{+2.89}_{-0.82}\times10^{45}$
F32	89	$2.015^{+0.236}_{-0.289}$	$2.61^{+0.70}_{-1.61}\times10^9$	$7.88^{+0.70}_{-0.68}\times10^{46}$	$5.93^{+0.79}_{-0.79}\times10^{45}$
F33	94	$2.058^{+0.299}_{-0.310}$	$3.68^{+1.93}_{-2.17}\times10^9$	$1.00^{+0.11}_{-0.08}\times10^{47}$	$4.74^{+2.11}_{-0.72}\times10^{45}$
F34	99	$2.053^{+0.258}_{-0.246}$	$4.76^{+2.80}_{-2.79}\times10^9$	$1.80^{+0.35}_{-0.58}\times10^{47}$	$8.83^{+4.46}_{-0.81}\times10^{45}$

3 ANALYSIS

For this study we measure the average SFRs of 3026 optical QSOs as a function of their bolometric luminosity and redshift. We use multiwavelength photometry covering the MIR–FIR wavelengths (12–500 μm) to perform SED fitting. With the sample of QSOs explored in this study we can extend the SFR–$L_{AGN,bol}$ plane of Stanley et al. (2015) by an order of magnitude in AGN luminosity, with 3026 sources covering the luminosities of $L_{AGN,bol} = 10^{45}$–10^{48} erg s^{-1}. Following Stanley et al. (2015), we have divided our sample in four redshift ranges, $z = 0.2$–0.5, 0.5–0.8, 0.8–1.5 and

1.5–2.5, which then are split in $L_{AGN,bol}$ bins of roughly equal number of sources (80–100 sources; see Table 1). For each z–$L_{AGN,bol}$ bin we performed stacking analysis in the *Herschel* PACS and SPIRE bands to estimate the mean 100, 160, 250, 350 and 500 μm fluxes (Section 3.1). We also calculate the mean 12 and 22 μm *WISE* fluxes (Section 3.2), and mean bolometric AGN luminosities from the optical data (see Section 2.2). We then used the mean fluxes of each z–$L_{AGN,bol}$ bin to perform composite SED fitting to decompose the IR luminosity into the AGN and star formation contributions (Section 3.3). The combination of the multiwavelength stacking and

SED fitting provides constraints on the mean IR luminosity due to star formation free from the possible AGN contamination, and the uncertainties of monochromatic estimations.

3.1 Stacking *Herschel* photometry

In this section we describe the methods followed to calculate the mean stacked flux density for each z–$L_{\rm AGN,bol}$ bin in our analysis. For each bin we perform a weighted mean stack of the H-ATLAS PACS 100 and 160 μm, and SPIRE 250, 350 and 500 μm images at the optical positions of the SDSS QSOs. In all cases we regrid the images to pixels of 1 arcsec, so as to have more accurate central positioning. We used the noise maps to define the weighting on the mean, by taking the inverse of the noise as the weight, to take into account that instrumental noise changes within the maps. The equation for the weighted mean of each pixel in the stacked image is

$$\langle x \rangle = \frac{\sum_0^n x_i \, w_i}{\sum_0^n w_i}, \tag{2}$$

where x is the flux density of a pixel in the stacked image, x_i is the flux density of the equivalent pixel at all images used in the stack and w_i is the inverted flux density at the equivalent pixel of the noise map. We note that the results do not change if we take w_i to be the inverse variance, with a difference of <2 per cent.

From the mean stacked image (see Fig. 4) we measure the mean flux density of each z–$L_{\rm AGN,bol}$ bin. For the PACS stacks, which are in units of Jy pixel^{-1}, we integrate the flux density within an aperture of 3 arcsec radius and use the recommended aperture corrections of 2.63 and 3.57 for 100 and 160 μm, respectively (Valiante et al. 2016). For the SPIRE stacks, which are in units of Jy beam^{-1}, we take the flux density of the central pixel.

To ensure that a stacked flux density measurement is significant, and above the noise, we perform random stacks within the image. Random stacks are stacks that are calculated for a number of random positions on the map. Because each bin includes a different number of sources from each field, we perform random stacks for each bin individually, and require that the number of random positions to be taken from each field is the same as that used to produce the stack image for the sources in the bin. We perform 10 000 random stacks of the maps following the same procedure as for the stack images of the sources, to create a distribution of randomly stacked values. Examples of the resulting random stack distributions for all the bands are shown in Fig. 4. The resulting random stack distributions for the SPIRE bands are not centred on zero, but are positively offset by typical values of 1.3, 2 and 0.5 mJy for the 250, 350 and 500 μm, respectively. The offset is caused by the fact that random stacks will include positive flux density from the confused background (i.e. blending of faint sources). These are taken into account for the science stacks below. We fit a Gaussian to each random stack distribution, and from the fit we calculate the σ of the distribution. We use the 3σ of the random-stack distribution plus the non-zero offset as our detection limit. If the stacked flux density measurement is above the defined limit, then it is a detection and we use its absolute value, if it is below the limit we take an upper limit equal to the 3σ value of the random stack distribution.

The offset of the random-stack distribution described above reflects a boosting in flux density from the confusion background that causes a boost in flux density of the individual bins. We therefore remove this offset from the stacked flux density in all bands for all z–$L_{\rm AGN,bol}$ bins. QSOs are well known for their clustering (e.g. White et al. 2012 and references therein), which may cause an additional boost to the stacked flux densities. In Wang et al. (2015) it was found that due to clustering of other dusty star-forming galaxies around optical QSOs there is an ∼8–13 per cent contamination to the 250–500 μm flux density, respectively. To place an estimate on the possible contamination due to neighbouring sources, we fit the radial light profile of the stacked images using a combination of the point spread function (PSF) model and a constant contamination factor constrained at longer radii (see Appendix B). We find that the contamination derived using our simple method is equivalent to the offsets found within the random stack distributions of our bins. Consequently, the contamination measured here is still only constraining the confusion background of our stacks. It is possible that there is additional contamination due to clustering that our method is not able to constrain. However, an additional contamination of ∼10 per cent in the SPIRE bands will not affect our final results on the IR luminosity by more than their 1σ uncertainties.

The uncertainties on the mean fluxes are estimated using the bootstrap technique. We perform 1000 re-samplings for each bin by randomly selecting 80 per cent of the sources in each bin, and calculate the mean flux density of each. From the resulting distribution of mean flux densities we can define the 1σ uncertainties by taking the 16th and 84th percentiles (see examples in Fig. 4).

3.2 Mean flux densities of the *WISE* counterparts

For each z–$L_{\rm AGN,bol}$ bin of our sample we took the mean flux densities at 12 and 22 μm for the sources with a *WISE* counterpart. The fraction of sources with upper limits in the 12 and 22 μm bands ranges in the z–$L_{\rm AGN,bol}$ bins, with a median of 1.3 and 32 per cent, respectively. When present the limits show a random enough distribution amongst the measured flux densities to allow us to use the non-parametric Kaplan–Meier estimator for the calculation of the mean of each bin, including both upper limits and measured flux densities (K–M method; e.g. Stanley et al. 2015; see Feigelson & Nelson 1985 for more details). We use this method for the estimation of the mean *WISE* fluxes in each bin of our sample. We chose this method over stacking the *WISE* photometry, as the source extraction that has been performed by the *WISE* team has taken into account of instrumental effects (Wright et al. 2010), providing good quality photometry. To test how the modest fraction of sources with *WISE* upper limits could affect the uncertainties on our estimations, we take two extreme cases, where all the upper limit sources are given a value of 0, and where all upper limit sources are assumed detections at that limit. We calculate the mean flux density for both approaches in all z–$L_{\rm AGN,bol}$ bins, and find that the range between the two approaches is less than 0.15 mJy in the 12 μm band and less than 2 mJy in the 22 μm band, and the mean calculated with the K–M method always lies within the range of these values. Based on this we trust that the K–M method is giving realistic results. We use bootstrap re-sampling to estimate the 1σ uncertainties on the means. We note that the bootstrap uncertainties on the mean fluxes are always smaller than the range estimated for the extreme cases above.

3.3 Composite SED fitting

In Fig. 5 we show how the *Herschel* bands cover the peak of the star-forming templates at the redshifts of interest, making them essential for the estimation of the SFRs. However, the AGN could also be contributing to the FIR fluxes of each bin, especially at higher redshifts (see Fig. 5). For this reason we perform SED fitting to the *WISE* 12 and 22 μm, PACS 100 and 160 μm and SPIRE
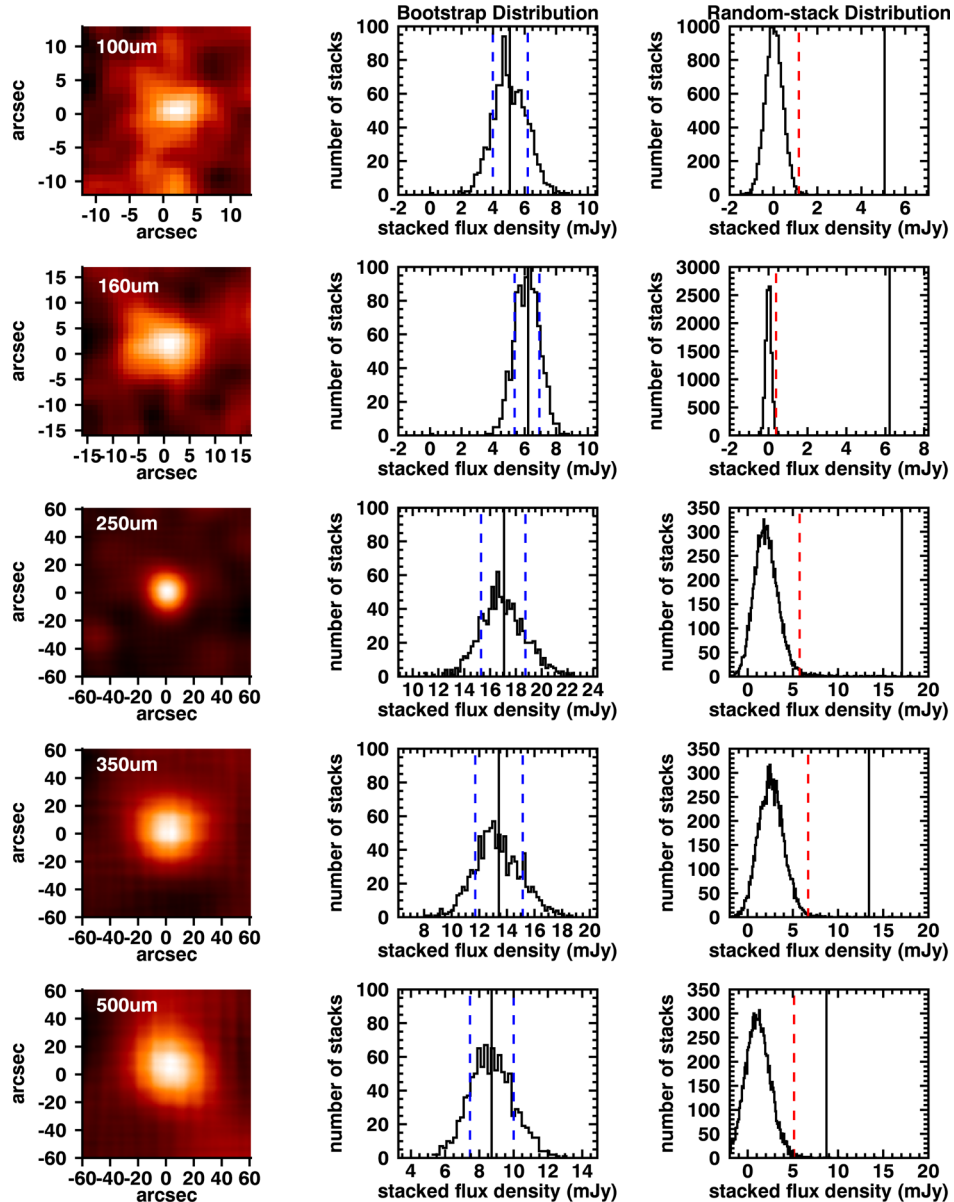
Figure 4. Examples of our stacking procedure for the PACS and SPIRE bands, corresponding to the z–$L_{\text{AGN,bol}}$ bin F33 of Table 1. First shown are the stacked images in 100, 160, 250, 350 and 500 μm, followed by the bootstrap and random-stack distributions. The bootstrap distribution is a result of randomly re-sampling the sources in the stacks and estimating the stacked mean flux density 1000 times. The mean flux density of the bin is shown with the black line, and in blue dashed lines we show the 16th and 84th percentiles that correspond to the 1σ uncertainty on the mean. The random-stack distribution is produced by stacking at random positions in the images, the number of which is defined by the number of sources in the bin. The 99.5th percentile ($\sim 3\sigma$; red dashed line) is the limit we use to define if a stacked flux density is significant (see Section 3.1).

250, 350 and 500 μm mean flux densities of each z–$L_{\text{AGN,bol}}$ bin, and decompose the AGN and star formation contributions to the IR luminosity.

We follow the methods described in Stanley et al. (2015), which we briefly outline here. We simultaneously fit an AGN template and a set of star-forming templates, and leave the normalization of the star-forming and AGN template as free parameters in the fit. The set of star-forming templates includes the five originally defined in Mullaney et al. (2011), extended by Del Moro et al. (2013) to cover a wider wavelength range (i.e. 3–10⁵ μm; however, for the purposes of our SED fitting we are only fitting within the 3–1000 μm wavelength region), and the Arp 220 galaxy template from Silva et al. (1998) (see Fig. 5). The AGN template used in

our fitting analysis was defined in Mullaney et al. (2011) based on a sample of X-ray AGN, and is shown in Fig. 5. For each z–$L_{\text{AGN,bol}}$ bin we perform two sets of SED fitting, one using only the six different star-forming templates, and the other using the combination of the AGN and the star-forming templates. Using the Bayesian information criterion (BIC) parameter (Schwarz 1978) to compare the two sets of fits, we determine if a fit requires the AGN component, and find that all of our bins require the presence of the AGN counterpart in their IR SEDs. The fit with the minimum BIC value is taken to be the best-fitting result. Examples of best-fitting SEDs for bins at the four different redshift ranges are given in Fig. 6; the resulting best-fitting SEDs for all the z–$L_{\text{AGN,bol}}$ bins are shown in Appendix A.
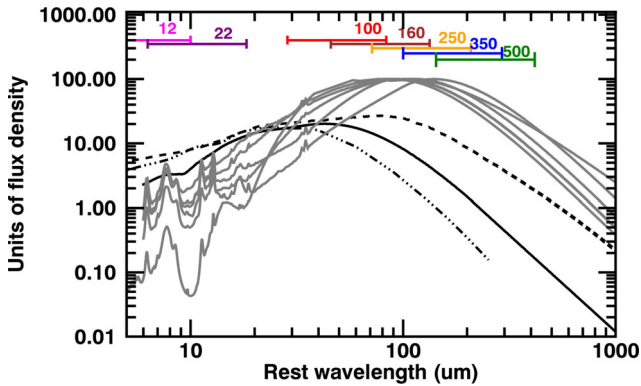
Figure 5. The normalized IR SED templates used in our analysis, for comparison, plotted in arbitrary units of flux density as a function of rest-frame wavelength. With grey curves we show the six star-forming galaxy templates that include the five templates derived by Mullaney et al. (2011) and Arp 220 derived by Silva et al. (1998), normalized to the peak flux density. With the black solid curve we show the mean AGN template of Mullaney et al. (2011) template, adopted in our analysis (see Section 3.3). Also plotted are two alternative AGN templates, used in Section 5.1.2, to test the effect of the choice of AGN template on our results. With the dot–dashed curve we show the AGN template of Mor & Netzer (2012), and with the dashed curve the AGN template of Symeonidis et al. (2016). In coloured horizontal lines we show the wavelength range of the SED covered by the W3 (12 μm) and W4(22 μm) *WISE* bands and the five FIR *Herschel* bands of 100, 160, 250, 350 and 500 μm at redshifts of 0.2–2.5. The 250 μm band covers the wavelengths where the star-forming galaxy templates peak for the full redshift range of this study. However, at $z \gtrsim 1$ it covers the wavelengths close to the peak of the AGN SED, and hence it could suffer from significant contamination from AGN emission if used as a monochromatic SFR indicator.

From the resulting best-fitting SEDs we calculate the mean IR luminosity due to star formation of each bin, $\langle L_{IR,SF} \rangle$, by integrating the star-forming component over 8–1000 μm. The same is also done to estimate the mean IR (8–1000 μm) luminosity of the AGN

($\langle L_{IR,AGN} \rangle$) of each bin. To determine the uncertainty on the $\langle L_{IR,SF} \rangle$ and $\langle L_{IR,AGN} \rangle$, we propagate the error on the fit and the range of luminosities of the fits within $\Delta BIC = BIC - BIC_{min} \leq 2$ that can be argued to be equally good fits to the best fit (e.g. Liddle 2004). From the calculated $\langle L_{IR,SF} \rangle$ values we estimate the corresponding mean SFR values by using the Kennicutt (1998) relation corrected for a Chabrier (2003) IMF. For both the SED fitting analyses and the calculation of the IR luminosities, we use the mean redshift of the sources in each z–$L_{AGN,bol}$ bin.

We can see from Fig. 6 that as we move towards higher redshifts the strong AGN component, present in all our fits, becomes increasingly dominant in the FIR bands. Indeed, as we show in Section 4.1 the AGN can contribute up to 60 per cent to the total IR flux density at redshifts of $z \sim 2$. However, as our SED fits show a strong AGN component, the results of this analysis will be dependent on the AGN template of choice.

As an initial test on the suitability of the AGN template of choice, we compare the bolometric AGN luminosity derived from our fitted AGN components to that derived from the optical. To do this we use the 6 μm rest-frame luminosity of the fitted AGN components of our bins, and convert to an AGN bolometric luminosity with a bolometric correction factor of 8 (following Richards et al. 2006). We find that the IR-derived bolometric AGN luminosity is consistent to the optical-derived bolometric AGN luminosity within a scatter of a factor of ∼1.5 around the '1–1' line. Consequently, we trust that the AGN template that we use is reliable for subtracting the AGN contribution to the total IR emission, and therefore for calculating the SFRs of this sample. To further verify our approach, in Section 5.1.2 we perform some additional tests using different AGN templates (from Mor & Netzer 2012; Symeonidis et al. 2016; see dot–dashed and dashed curves in Fig. 5) to evaluate the effect the choice of AGN template has on our results. We find that our choice of AGN template is fair and our results will not change significantly for different AGN templates.

To examine if different selection methods could affect the shape of our resulting composite SEDs we have split each z–$L_{AGN,bol}$ bin
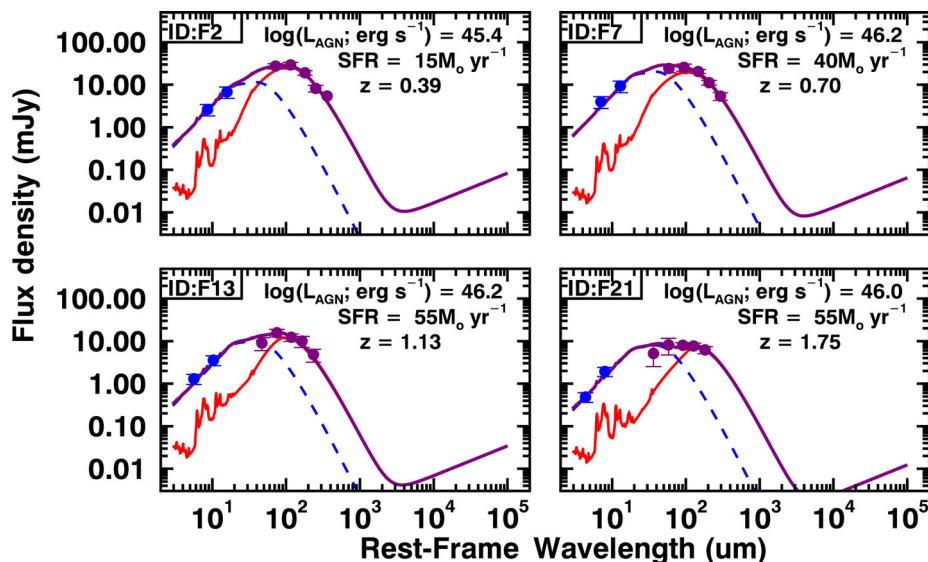

Figure 6. Examples of the SED fits from four $L_{AGN,bol}$–z bins, one from each of the four redshift ranges (i.e. $z = 0.2$–0.5, 0.5–0.8, 0.8–1.5 and 1.5–2.5), for the full QSO sample. The blue data points correspond to the mean flux density of *WISE* bands W3 and W4, while the purple data points correspond to the mean flux density of PACS 100 and 160 μm and SPIRE 250, 350 and 500 μm bands. The blue dashed curve is the best-fitting AGN template, the red solid curve is the best-fitting star-forming template and the purple solid curve is the resulting overall SED (see Section 3.3 for details on the SED fitting analysis). The AGN emission can significantly contribute to the PACS and SPIRE bands, especially at $z \gtrsim 1$.

based on two different selections, and repeat the stacking and SED fitting analysis described in this section. First we have used the *WISE* colour classification of Stern et al. (2012) for MIR AGN, and find that the majority of sources in the bins (ranging between ~49 and 98 per cent for the different bins) are selected as MIR AGN. The resulting composite SEDs of the MIR AGN selected subsample, as well as the resulting $\langle L_{\mathrm{IR,SF}} \rangle$ values, are consistent to those of the overall sample within a factor of 1.2 for 30/34 of the bins, while the rest lie within a factor of 2–3.3. A second selection was based on whether or not a source is detected at 250 μm in the 5σ point source catalogue of Valiante et al. (2016),[3] thus selecting FIR luminous sources. Unsurprisingly the majority of our sample is undetected in the FIR, with only 8–19 FIR detected sources in each bin. The resulting composite SEDs of the FIR undetected subsamples, as well as the resulting $\langle L_{\mathrm{IR,SF}} \rangle$ values, are consistent to those of the overall sample, supporting the idea that the few FIR luminous sources in each bin are not driving the means significantly (something also demonstrated by the bootstrap distributions of our stacks; see Fig. 4). Overall, we find that our mean composite SEDs are representative of the full sample and their shape, i.e. the combination of strong AGN and star-forming components is still seen when splitting the sample on the MIR or FIR properties, and are not driven by biases caused by MIR or FIR bright sources.

The method followed in this study is significantly different to the one favoured by a number of previous studies performed with H-ATLAS (e.g. Hardcastle et al. 2013; Kalfountzou et al. 2014; Gürkan et al. 2015). In those studies the authors have been using monochromatic 250 μm luminosities to derive SFRs, where the other FIR bands are used to derive the temperature of the modified blackbody SED using FIR colours. As this method does not take into account the AGN emission at FIR wavelengths, there is a level of uncertainty on the IR luminosity due to star formation, as there is possible AGN contamination; see Section 4.1. However, as discussed in Sections 4.2 and 4.3 our results are in general agreement with the SFR values reported in previous work, including those mentioned above.

4 RESULTS

Here we present the main results of our study on the mean SFRs of QSOs, following the analysis presented in Section 3. Initially, we compare our results of mean SFRs from our composite SEDs, to those from a monochromatic derivation at 250 μm (Section 4.1). We then investigate the SFR properties of our full QSO sample (Section 4.2), and the radio-luminous subsample (Section 4.3).

4.1 Multiband SED fitting versus single-band derivation for the calculation of star formation luminosities

A common method of previous studies in estimating the SFRs of AGN and QSOs is using stacking at observed frame 250 μm from which the IR luminosity and SFRs are then inferred (e.g. Harrison et al. 2012; Kalfountzou et al. 2014; Gürkan et al. 2015). In this section we compare our results from the multiwavelength composite SED fitting to the single band 250 μm derivation, where we do not take into account the contribution from the AGN. To derive the average IR luminosities (integrated over rest-frame 8–1000 μm)
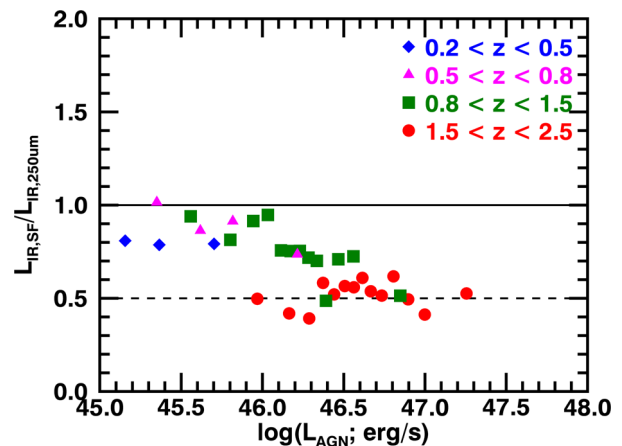
Figure 7. A comparison of the resulting mean IR luminosity due to star formation from our composite SED fitting method ($\langle L_{\mathrm{IR,SF}} \rangle$), compared to the single-band derivation of the IR luminosity from the 250 μm band ($L_{\mathrm{IR,250\,\mu m}}$). The solid line corresponds to the 1–1 line, and the dashed line is a factor of 2 offset from that. We find that the 250 μm band starts to be strongly contaminated by the AGN emission for high-luminosity AGN ($L_{\mathrm{AGN,bol}} \gtrsim 10^{46}$ erg s^{-1}) and at high redshifts ($z \gtrsim 1$).

from the 250 μm stacked fluxes, we normalize from the six star-forming galaxy templates that we used in our SED fitting method (see Fig. 5 and Section 3.3), to the mean flux density at 250 μm, and take the mean of the resulting IR luminosities of the six star-forming galaxy templates (referred to as $L_{\mathrm{IR,250\,\mu m}}$).

In Fig. 7 we compare the results of the two methods described above: (1) the mean IR luminosity derived from the observed frame 250 μm photometry and (2) the multiwavelength SED fitting and decomposition method followed in our analyses. We find that for redshifts of $z \lesssim 0.5$ a single-band derivation from the 250 μm band is not affected significantly by the AGN, with a median offset of a factor of 1.2. At redshifts of $z \gtrsim 0.5$ we see a more luminosity-dependent effect, with the $L_{\mathrm{IR,250\,\mu m}}$ being affected by the AGN by an increasing factor with AGN luminosity, reaching up to a factor of ≈2 overestimation at the highest luminosities ($L_{\mathrm{AGN,bol}} > 10^{46}$ erg s^{-1}). At the highest redshifts of $z \sim 2$ the $L_{\mathrm{IR,250\,\mu m}}$ is consistently overestimated by a factor of 2–2.5. Similar results on the contribution of the AGN to the total IR luminosity have also been found for higher redshift QSOs ($z \sim 6$; see Schneider et al. 2015).

4.2 The mean SFRs of optical QSOs as a function of the bolometric AGN luminosity

As described in Section 3, we split our sample in bins of redshift and $L_{\mathrm{AGN,bol}}$, for which we then estimate the mean $L_{\mathrm{IR,SF}}$ ($\langle L_{\mathrm{IR,SF}} \rangle$) through multiwavelength stacking and SED fitting that decomposes the AGN and star-forming components.

In Fig. 8(a) we present our results on $\langle L_{\mathrm{IR,SF}} \rangle$ as a function of $L_{\mathrm{AGN,bol}}$ and redshift. We see a positive trend of the $\langle L_{\mathrm{IR,SF}} \rangle$ as a function of $L_{\mathrm{AGN,bol}}$ of more than an order of magnitude, something also observed in previous studies (e.g. Bonfield et al. 2011 Rosario et al. 2013; Kalfountzou et al. 2014; Karouzos et al. 2014; Gürkan et al. 2015). However, when splitting in redshift ranges, we find that the observed trend is largely due to the redshift evolution of typical SFR values. Within each redshift range we still see a slight positive trend of $\langle L_{\mathrm{IR,SF}} \rangle$ with $L_{\mathrm{AGN,bol}}$, with the factor of increase ranging from ~1.6 to 6.3 (0.2 to 0.8 dex), with the highest redshift range of $1.5 < z < 2.5$ showing the largest increase with $L_{\mathrm{AGN,bol}}$.
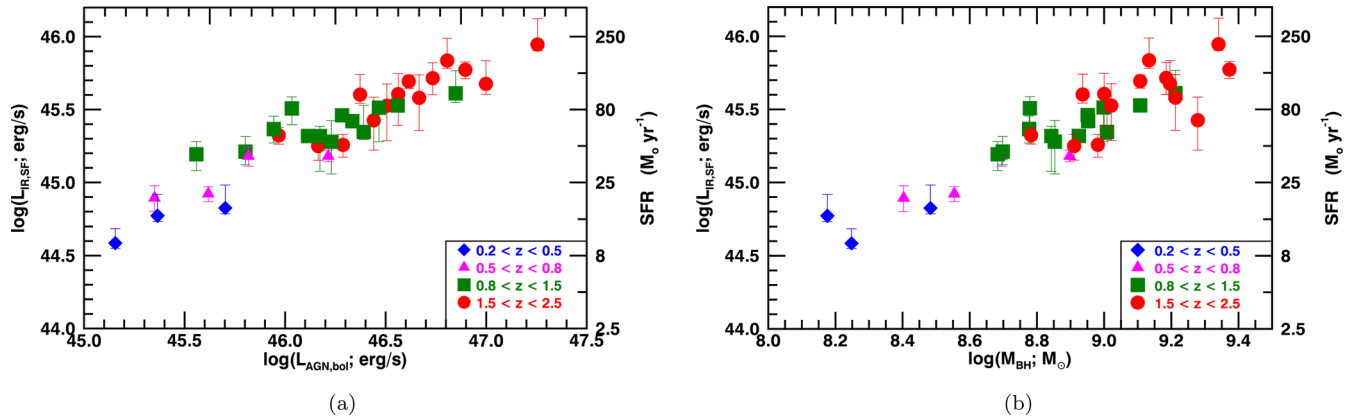
(a)   (b)

Figure 8. (a) $\langle L_{\rm IR,SF} \rangle$ as a function of AGN bolometric luminosity ($L_{\rm AGN,bol}$). The coloured filled symbols show the results for the full QSO sample in z–$L_{\rm AGN,bol}$ bins. (b) $\langle L_{\rm IR,SF} \rangle$ as a function of the mean BH mass ($\langle M_{\rm BH} \rangle$) of each z–$L_{\rm AGN,bol}$ bin. Also provided are the corresponding SFR values estimated using the Kennicutt (1998) relation corrected to a Chabrier IMF (Chabrier 2003). A slight trend of increasing $\langle L_{\rm IR,SF} \rangle$ with $L_{\rm AGN,bol}$ is seen for the QSO sample, this positive trend is also seen between the $\langle L_{\rm IR,SF} \rangle$ and $M_{\rm BH}$. We argue that the positive trend of $\langle L_{\rm IR,SF} \rangle$ with $L_{\rm AGN,bol}$ observed in this sample is mainly driven by mass dependencies (see Section 5.2.1).

In Fig. 8(b) we show the $\langle L_{\rm IR,SF} \rangle$ as a function of the mean BH mass ($\langle M_{\rm BH} \rangle$) of each bin, and see a positive trend of the $\langle L_{\rm IR,SF} \rangle$ with $\langle M_{\rm BH} \rangle$ at all redshifts. This is in agreement with the results of Harris et al. (2016) on QSOs at higher redshifts ($2 < z < 3$). Since the BH masses and stellar masses of the galaxies correlate (e.g. Kormendy & Ho 2013), an increase in $M_{\rm BH}$ likely reflects an increase in stellar mass. Consequently, the observed positive trend of the $\langle L_{\rm IR,SF} \rangle$ with $L_{\rm AGN,bol}$ (Fig. 8a) could also be a result of increasing stellar masses (i.e. as seen for the star-forming galaxy population; e.g. Schreiber et al. 2015) rather than AGN luminosity. We explore this further in Section 5.2.1.

In our previous work (Stanley et al. 2015) we constrained the $\langle L_{\rm IR,SF} \rangle$ for a sample of X-ray AGN in bins of redshift and $L_{\rm AGN,bol}$. The sample of X-ray AGN covers three orders of magnitude in $L_{\rm AGN,bol}$ of both moderate and high-luminosity AGN ($10^{43} < L_{\rm AGN,bol} < 5 \times 10^{47}$ erg s^{-1}). The sample of high-luminosity optical QSOs in this work is ideal to extend the $\langle L_{\rm IR,SF} \rangle$–$L_{\rm AGN,bol}$ plane as defined in Stanley et al. (2015) to the highest $L_{\rm AGN,bol}$ region. It also allows us to search for systematic differences between the two populations of AGN. In Fig. 9 we plot the $\langle L_{\rm IR,SF} \rangle$ as a function of $L_{\rm AGN,bol}$ for both the X-ray AGN and optical QSOs extending the $\langle L_{\rm IR,SF} \rangle$–$L_{\rm AGN,bol}$ plane to four orders of magnitude. Where there is overlap in AGN luminosity between the X-ray selected AGN sample of Stanley et al. (2015) and our current sample of optical QSOs, we see a good agreement in $\langle L_{\rm IR,SF} \rangle$ values.[4] At the highest redshift range of $1.5 < z < 2.5$ the $\langle L_{\rm IR,SF} \rangle$ values of four bins at $\log L_{\rm AGN,bol} < 46.4$ of our QSO sample seem in disagreement to

---

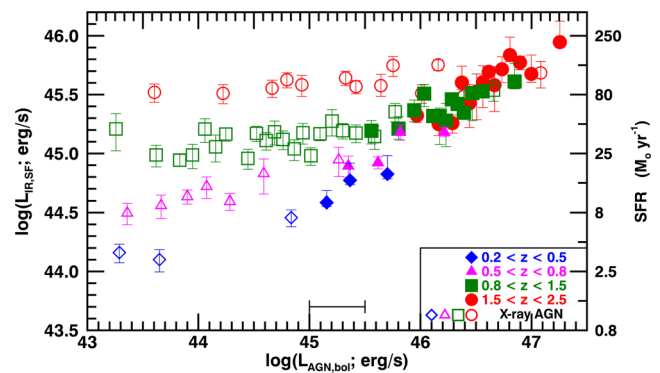[4] We note that there is a relative uncertainty between AGN bolometric luminosities when calculated from different photometry. To estimate the possible uncertainty between the estimates of the bolometric luminosity of our optical QSOs and the X-ray AGN sample of Stanley et al. (2015), we use 2XMM to SDSS DR7 cross-correlated catalogue from Pineau et al. (2011). We take the X-ray hard band flux density and calculate a bolometric luminosity, and compare to the bolometric luminosity from the optical measurements. We take the ratio of the two, and find that there is a median offset of 3.6 (or 0.56 dex). However, despite the uncertainty on comparing these samples, the observed trends will not be significantly affected. As this is a different sample to those we compare here, and there is no definitively correct bolometric luminosity correction, we do not apply this correction, but we do indicate it in Fig. 9.

Figure 9. $\langle L_{\rm IR,SF} \rangle$ as a function of AGN bolometric luminosity ($L_{\rm AGN,bol}$) for the combination of the X-ray AGN sample from Stanley et al. (2015) and the current sample of optical QSOs. The redshift ranges of the X-ray AGN sample are the same as those of our sample and have been colour coded to match. Also provided are the corresponding SFR values estimated using the Kennicutt (1998) relation corrected to a Chabrier IMF (Chabrier 2003). The two samples are complementary to each other, and together cover 3–4 orders of magnitude in $L_{\rm AGN,bol}$. We indicate the 0.5 dex systematic uncertainty between the $L_{\rm AGN,bol}$ values of the two samples as a range over the x-axis, stemming from the fact that the X-ray AGN sample has $L_{\rm AGN,bol}$ values derived from X-ray photometry, while for the QSO sample it has been derived from optical photometry (see Footnote 3).

those of the X-ray AGN, although they are still consistent within the scatter of the X-ray AGN sample in that redshift range. However, in this comparison the two samples have not been matched in stellar mass, and this may drive some of the differences between the $\langle L_{\rm IR,SF} \rangle$ values (see Section 5.2.1 for a discussion on the effect of mass on the expected $\langle L_{\rm IR,SF} \rangle$ values). Overall, this comparison shows that the two populations of AGN have consistent mean SFRs at fixed $L_{\rm AGN,bol}$, and that the $\langle L_{\rm IR,SF} \rangle$ values as a function of $L_{\rm AGN,bol}$ of our sample complement and extend the trends observed for the X-ray AGN sample.

4.3 The mean SFRs of radio-luminous QSOs

In parallel to our analysis of the full sample of QSOs, we also analysed a subsample of radio-luminous QSOs selected based on a radio luminosity ($L_{\rm 1.4\,GHz}$) cut (see Fig. 2 and Section 2.3). As

Table 2. The mean source properties for each z–$L_{1.4\,\mathrm{GHz}}$ bin in our subsample of radio-luminous QSOs. Column (1): the ID of the bin that corresponds to the set of SEDs presented in the appendix. Column (2): the number of sources in each bin. Column (3): the mean redshift of each bin. Column (4): the mean BH mass of each bin. Column (5): the mean radio luminosity at 1.4 GHz. Column (6): the mean AGN bolometric luminosity (derived from the optical) of each bin. The uncertainties in columns (3), (4), (5) and (6) correspond to the 16th–84th percentiles of the values in each bin. Column (7): the mean IR luminosity due to star formation from the best-fitting SED of each bin, the uncertainties are defined by the combination of the error on the fit and the range of $\langle L_{\mathrm{IR,SF}} \rangle$ values from other templates that had good SED fits (see Section 3.3).

| ID	N	$\langle z \rangle$	$\langle M_{BH} \rangle$ $(M_{\odot})$	$\langle L_{1.4\,\mathrm{GHz}} \rangle$ (W Hz^{-1})	$\langle L_{\mathrm{AGN,\,bol}} \rangle$ (erg s^{-1})	$\langle L_{\mathrm{IR,\,SF}} \rangle$ (erg s^{-1})
(1)	(2)	(3)	(4)	(5)	(6)	(7)
R1	17	$0.663^{+0.131}_{-0.074}$	$1.27^{+2.40}_{-1.07} \times 10^9$	$0.45^{+0.48}_{-0.22} \times 10^{25}$	$1.00^{+3.44}_{-0.84} \times 10^{46}$	$2.60^{+0.55}_{-1.30} \times 10^{45}$
R2	15	$0.710^{+0.076}_{-0.080}$	$1.52^{+2.99}_{-1.25} \times 10^9$	$0.94^{+2.16}_{-0.81} \times 10^{26}$	$1.22^{+1.67}_{-0.98} \times 10^{46}$	$1.00^{+0.17}_{-0.17} \times 10^{45}$
R3	53	$1.131^{+0.243}_{-0.187}$	$1.91^{+2.10}_{-1.56} \times 10^9$	$0.40^{+0.33}_{-0.22} \times 10^{26}$	$1.99^{+1.68}_{-1.45} \times 10^{46}$	$4.07^{+0.96}_{-2.18} \times 10^{45}$
R4	50	$1.180^{+0.192}_{-0.218}$	$1.52^{+0.97}_{-1.20} \times 10^9$	$2.46^{+0.27}_{-2.35} \times 10^{27}$	$3.05^{+1.60}_{-2.27} \times 10^{46}$	$5.17^{+1.07}_{-0.89} \times 10^{45}$
R5	54	$1.913^{+0.308}_{-0.286}$	$2.28^{+1.12}_{-1.69} \times 10^9$	$0.87^{+1.05}_{-0.64} \times 10^{26}$	$5.77^{+4.89}_{-4.31} \times 10^{46}$	$3.12^{+1.48}_{-1.36} \times 10^{45}$
R6	49	$1.882^{+0.394}_{-0.321}$	$2.68^{+2.65}_{-1.98} \times 10^9$	$2.84^{+0.76}_{-2.39} \times 10^{27}$	$7.92^{+8.13}_{-5.99} \times 10^{46}$	$4.17^{+0.87}_{-0.61} \times 10^{45}$
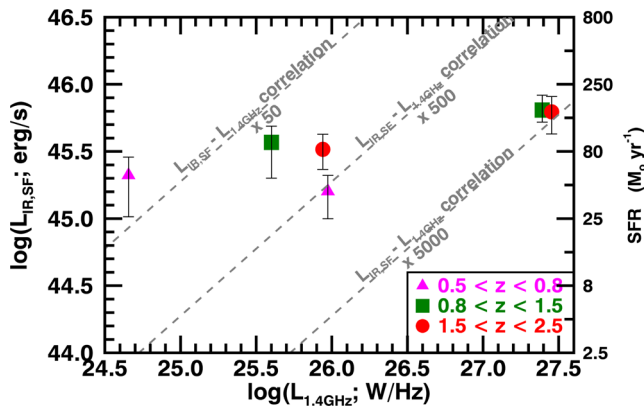
Figure 10. $\langle L_{\mathrm{IR,SF}} \rangle$ in bins of redshift and radio luminosity ($L_{1.4\,\mathrm{GHz}}$) as a function of $\langle L_{1.4\,\mathrm{GHz}} \rangle$. Also provided are the corresponding SFR values estimated using the Kennicutt (1998) relation corrected to a Chabrier IMF (Chabrier 2003). With dashed lines we indicate the IR–radio relation of star-forming galaxies from Magnelli et al. (2014) increased by factors of 50–5000, to demonstrate that the radio luminosities of our sources cannot be attributed to their star formation. There is no strong evidence for a positive or negative relation between $\langle L_{\mathrm{IR,SF}} \rangle$ and $L_{1.4\,\mathrm{GHz}}$, with the general trend being flat. However, for the higher $L_{1.4\,\mathrm{GHz}}$ bins of each redshift range the $\langle L_{\mathrm{IR,SF}} \rangle$ could be highly contaminated by synchrotron emission, and therefore these results are uncertain.

we show below, the radio luminosities of our sample are at least an order of magnitude above those corresponding to the $\langle L_{\mathrm{IR,SF}} \rangle$ of our bins, and so we are confident that these radio luminosities are dominated by emission associated with the AGN and not the star formation. For each redshift range we split the sample in $L_{1.4\,\mathrm{GHz}}$ bins of roughly equal numbers ($\sim$15–54; see Table 2). Because of the limited number of sources we can only have two bins in each redshift range. For each bin we follow the procedures described in Section 3 to estimate $\langle L_{\mathrm{IR,SF}} \rangle$.

In Fig. 10 we plot $\langle L_{\mathrm{IR,SF}} \rangle$ as a function of $L_{1.4\,\mathrm{GHz}}$ in each bin. We also plot the IR–radio correlation for star-forming galaxies (from Magnelli et al. 2014; Pannella et al. 2015) multiplied by factors of 50, 500 and 5000, to demonstrate how the radio luminosities of our sample are a factor of $\sim$10–5000 above those corresponding to their $\langle L_{\mathrm{IR,SF}} \rangle$ values. In agreement with previous results on radio selected AGN (e.g. Seymour et al. 2011; Drouart et al. 2014, 2016; Kalfount-

zou et al. 2014; Karouzos et al. 2014; Magliocchetti et al. 2014; Gürkan et al. 2015; Podigachoski et al. 2016), we find that the radio-luminous QSOs of our sample live in galaxies with significant on-going star formation. Even though we only have two luminosity bins in each redshift range, the $\langle L_{\mathrm{IR,SF}} \rangle$ values as a function of $\langle L_{1.4\,\mathrm{GHz}} \rangle$ are suggestive of a flat trend, further implying that the radio luminosity does not originate from the star formation in these systems and also indicating the lack of a direct relationship between the star formation emission of the galaxy and the radio emission of the QSOs. This is also found in previous studies with different sample selections to ours, such as Seymour et al. (2011) and Drouart et al. (2016).

When comparing the radio-luminous QSOs to the overall QSO sample (dominated by radio-quiet QSOs), the $\langle L_{\mathrm{IR,SF}} \rangle$ values are consistent within scatter, and show similar trends with redshift. This result is also in agreement with previous work by Kalfountzou et al. (2014), comparing radio-loud to radio-quiet QSOs, at similar redshifts and $L_{\mathrm{AGN,bol}}$.

However, in our SED fitting analyses we do not take into account of the synchrotron component that can be present for radio-luminous QSOs. Consequently, our results on the $\langle L_{\mathrm{IR,SF}} \rangle$ could still be contaminated by synchrotron emission due to the AGN. Assuming a conservative spectral index of $\alpha = 0.5$, we take the 1.4 GHz flux density of the sources in each bin and integrate over 8–1000 µm to calculate the total IR luminosity due to synchrotron emission for each source. We compare the mean for each z–$L_{1.4\,\mathrm{GHz}}$ bin to the corresponding $\langle L_{\mathrm{IR,SF}} \rangle$ values and find that the lower $L_{1.4\,\mathrm{GHz}}$ bins of each redshift range are contaminated by <10 per cent, but the higher $L_{1.4\,\mathrm{GHz}}$ bins of each redshift range can be contaminated by 30–100 per cent making them highly uncertain, with the most uncertain bins having $L_{1.4\,\mathrm{GHz}} > 10^{27}$ W Hz^{-1}. More detailed analyses using multiwavelength radio photometry to constrain the spectral index of the sources is required to best constrain these results.

5 DISCUSSION

In this section we explore the caveats in our method and the possible implications on our results (Section 5.1). Following this, we discuss the possible drivers of the weak positive trends of the mean SFR with AGN luminosity seen in our results (Section 5.2).

5.1 Verification of our methods

5.1.1 SED broadening

In our SED fitting approach we assume that the observed-frame wavelengths correspond to the rest-frame wavelength of the mean redshift of a given z–$L_{\rm AGN,bol}$ bin, for all of the sources within the bin. That is, we do not take into account modest k-corrections due to the different redshifts of the sources within the stack. This may result in some broadening of the average SED that we did not take into account. However, as our z–$L_{\rm AGN,bol}$ bins have fairly narrow redshift ranges (see Tables 1 and 2) and there is a fairly even scatter around the mean redshift of the bins, we expect that overall there should not be significant broadening effects. To test this, we shift each of our AGN and star-forming templates to the redshift of each source in our z–$L_{\rm AGN,bol}$ bins. For each z–$L_{\rm AGN,bol}$ bin we then take the mean of all the redshifted SED templates to get a mean SED shape, and compare to the original SED template shifted at the mean redshift of the z–$L_{\rm AGN,bol}$ bin. We find that the shape of the mean redshifted SED templates is the same to the original template when shifted to the mean redshift, apart from some smoothing of the polyciclic aromatic hydrocarbon (PAH) features of the star-forming templates. Consequently, our results on $\langle L_{\rm IR,SF} \rangle$ are not affected by SED broadening effects.

5.1.2 The choice of AGN template

Since the resulting composite SEDs of our sample show such a strong AGN component, our results may be sensitive to the AGN template that we assume. For this reason, we repeat our analysis using two different AGN templates, that of Mor & Netzer (2012) and that of Symeonidis et al. (2016). The template of Mor & Netzer (2012), derived from a QSO sample with similar methods to Mullaney et al. (2011), has a steeper drop-off at longer wavelengths compared to our default template (see dot–dashed curve in Fig. 5). The Symeonidis et al. (2016) template, also derived from a QSO sample, has a more gradual drop-off at longer wavelengths compared to our default template (see dashed curve in Fig. 5). The varying contribution of the AGN template at longer wavelengths may affect the $\langle L_{\rm IR,SF} \rangle$ values estimated by our SED fitting approach.

In the first case, fitting with the Mor & Netzer (2012) AGN template we find that over all z–$L_{\rm AGN,bol}$ bins the results on the $\langle L_{\rm IR,SF} \rangle$ do not change significantly, with a maximum increase in $\langle L_{\rm IR,SF} \rangle$ of a factor of ≈ 1.2, and all bins remaining consistent within the 1σ to the original $\langle L_{\rm IR,SF} \rangle$ results. In the second case where we fit using the Symeonidis et al. (2016) AGN template, we find that up to redshifts of 1.5, the results from using the two templates are consistent within our estimated 1σ errors. However, at the highest 1.5–2.5 redshift range, the results using the Symeonidis et al. (2016) template show a much larger scatter to that of our original results, and show no sign of the correlation observed in our original results. Overall, the $\langle L_{\rm IR,SF} \rangle$ values resulting from fitting with the Symeonidis et al. (2016) template are within a factor of 3 for 31/34 of the z–$L_{\rm AGN,bol}$, with the remaining 3/34 bins, that are in the highest redshift range showing a difference of a factor of ~ 8. This result highlights that our results for the highest redshift range are the most sensitive to the choice of AGN template used in the SED fitting analysis. However, in the very recent studies of Lani, Netzer & Lutz (2017) and Lyu & Rieke (2017), which looked at the IR AGN SED of PG quasars following a similar approach to that of Symeonidis et al. (2016), it was found that the IR AGN SED has a steeper drop-off at long wavelengths than that argued for in Symeonidis et al. (2016). In-

deed, the shape is more similar to that of the Mullaney et al. (2011) and Mor & Netzer (2012) AGN templates. Consequently, even though our highest redshift range is the most sensitive in the AGN template of choice, it is not likely that our results are as strongly affected as the use of a Symeonidis et al. (2016)-type template would suggest.

5.2 Understanding the observed trends between the mean SFR and AGN properties

5.2.1 Comparing to the main sequence of star-forming galaxies

The main sequence of star-forming galaxies is defined from the observed correlation between SFR and stellar mass, and has been found to evolve with redshift (e.g. Noeske et al. 2007; Elbaz et al. 2011; Schreiber et al. 2015). Consequently, the SFR of a normal star-forming galaxy will be dependent on its stellar mass and redshift. In this subsection we test the simple hypothesis that on average QSOs lie on the main sequence of star-forming galaxies. This follows from Stanley et al. (2015), where we showed that when taking into account of the stellar masses and redshifts of the X-ray AGN sample, their mean SFRs are consistent with the main sequence of star-forming galaxies. By comparing our results to the mean SFRs of main-sequence galaxies with the same redshift and stellar masses, we can test if the QSO sample shows systematic differences to the overall star-forming population. Furthermore, we can determine if the trends we observe are simply driven by the galaxy properties.

For each z–$L_{\rm AGN,bol}$ bin of our sample we use the BH masses and redshifts of the individual sources to estimate the IR luminosity of main-sequence galaxies ($\langle L_{\rm IR,MS} \rangle$) corresponding to the properties of each. We use equation (9) of Schreiber et al. (2015) to calculate the $L_{\rm IR,MS}$:

$$\log_{10}(\text{SFR}_{\rm MS}[\text{ M}_\odot\text{ yr}^{-1}]) = m - 0.5 + 1.5r$$
$$- 0.3[\max(0, m - 0.36 - 2.5r)]^2, \qquad (3)$$

where $r = \log_{10}(1 + z)$, $m = \log_{10}(M_\star/10^9\,\text{M}_\odot)$, and $L_{\rm IR,MS} = \text{SFR}_{\rm MS}/4.5 \times 10^{-44}$ (we note that Schreiber et al. 2015 assume a Salpeter IMF for equation 3 that we take into account here). The 1σ scatter in the relation is ± 0.3 dex and remains out to at least a redshift of ~ 4 (Schreiber et al. 2015). As can be seen in the above equation, to estimate the $\langle L_{\rm IR,MS} \rangle$ we need a measurement of the stellar masses of our sample. As our sample consists of QSOs, where the QSO emission overpowers that of the host galaxy in the optical, it is very unreliable to use SED fitting methods to the optical photometry to calculate stellar masses. However, BH masses are available for all of the QSOs in our sample from Shen et al. (2011) (see Section 2.1), and can be used to infer stellar masses. To convert the BH masses to stellar masses we make use of the equation defined in Bennert et al. (2011), which includes an empirically derived redshift evolution term for redshifts of $z \lesssim 2$:[5]

$$\log_{10} \frac{M_{\rm BH}}{10^8\,\text{M}_\odot} = 1.12 \log_{10}\left(\frac{M_*}{10^{10}\,\text{M}_\odot}\right) + (1.15 \pm 0.15)$$
$$\times \log_{10}(1 + z) - 0.68 + (0.16 \pm 0.06). \qquad (4)$$

---

[5] We remind readers that in this paper we assume a Chabrier IMF, the same is assumed in Bennert et al. (2011). However, the equation defining the main sequence of star-forming galaxies is defined for a Salpeter IMF. For this reason we multiply the stellar masses calculated using equation (4) by a factor of 1.8 to correct to a Salpeter IMF (Bruzual & Charlot 2003) in order to use in equation (3).
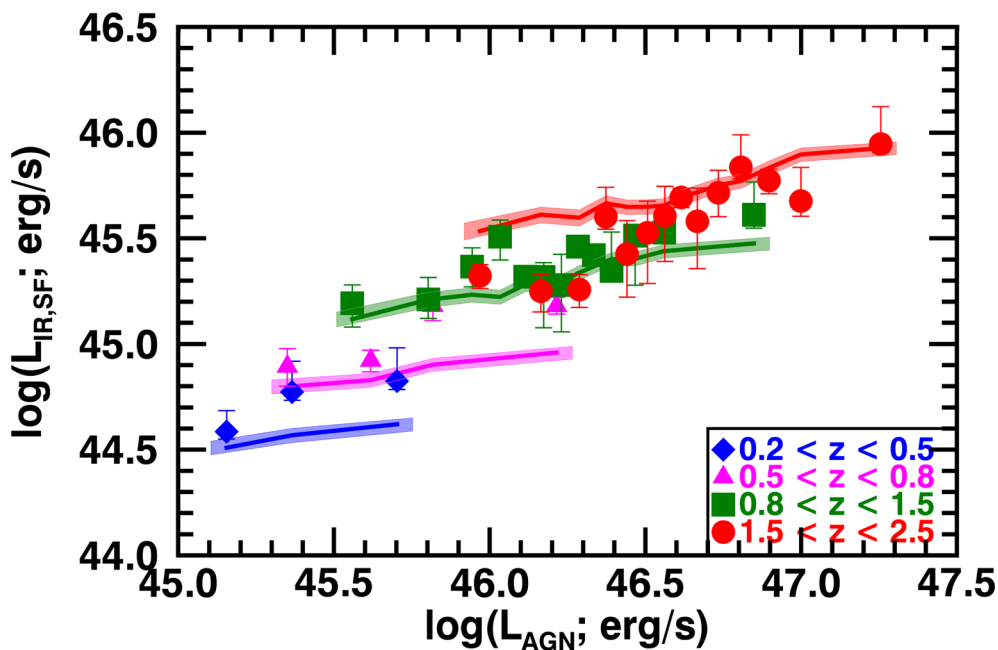
Figure 11. $\langle L_{IR,SF} \rangle$ as a function of $L_{AGN,bol}$ for the full QSO sample. The coloured regions indicate the expected range in $\langle L_{IR,MS} \rangle$ covered by the main-sequence galaxies at the stellar mass (as estimated from the M_{BH}) at each of the redshift ranges; the range reflects the bootstrap error on the $\langle L_{IR,MS} \rangle$ (see Section 5.2.1 for details on defining $\langle L_{IR,MS} \rangle$ and the error calculation). The observed trends between $\langle L_{IR,SF} \rangle$ and $L_{AGN,bol}$ are comparable to those of the $\langle L_{IR,MS} \rangle$, which is dependent on redshift and stellar mass (here inferred from the BH mass). Consequently, we argue that redshift and BH mass dependencies being the primary drivers of the observed trends of $\langle L_{IR,SF} \rangle$ with $L_{AGN,bol}$.

To establish if our optical QSOs are consistent with being a randomly selected sample from the main sequence of star-forming galaxies, we follow a similar approach to Rosario et al. (2013). For each z–$L_{AGN,bol}$ bin, we perform a Monte Carlo (MC) calculation of the $\langle L_{IR,MS} \rangle$ corresponding to the redshifts and masses of the sources in the bin. Using equation (4), we define a distribution of possible stellar masses for each QSO based on their BH mass, and pick a random value from the distribution. The width of the stellar mass distribution includes both the scatter in equation (4) and the error on the BH mass (provided by Shen et al. 2011; see Section 2.1). Based on the chosen stellar mass, and the known redshift of the source we define a lognormal distribution of $L_{IR,MS}$ values centred at the luminosity from equation (3), with a σ of 0.3 dex (Schreiber et al. 2015). We pick a random value from the distribution of $L_{IR,MS}$ values for the source. We repeat this approach for all sources in a z–$L_{AGN,bol}$ bin and then calculate the $\langle L_{IR,MS} \rangle$ of the bin. The above process is repeated 10 000 times for each bin, and results in a distribution of $\langle L_{IR,MS} \rangle$ from which we can define the mean and 1σ range of the possible $\langle L_{IR,MS} \rangle$ values for a given z–$L_{AGN,bol}$ bin.

In Figs 11 and 12 we plot the results for $\langle L_{IR,MS} \rangle$ in comparison to the $\langle L_{IR,SF} \rangle$ of the QSO sample. In Fig. 11 we plot $\langle L_{IR,SF} \rangle$ as a function of $L_{AGN,bol}$ in comparison to the results for main sequence star-forming galaxies for each redshift range. With the coloured lines we show the $\langle L_{IR,MS} \rangle$, and the coloured shaded regions correspond to the 1σ uncertainty on $\langle L_{IR,MS} \rangle$ distribution for each bin from our MC calculation. Additionally, we take the ratio of the $\langle L_{IR,SF} \rangle$ from our analysis over that of the main sequence ($\langle L_{IR,MS} \rangle$). We show the $\langle L_{IR,SF} \rangle / \langle L_{IR,MS} \rangle$ ratio as a function of $L_{AGN,bol}$ in Fig. 12(a), propagating the errors of the two variables. With the line we show the expected ratio for the main sequence, while the dashed lines indicate the range covered by the scatter of the main sequence relation as defined by Schreiber et al. (2015). From these two figures we can see an apparent trend in the $\langle L_{IR,SF} \rangle$

values of QSOs relative to those of the main sequence star-forming galaxies, as a function of redshift. At the highest redshift range of $1.5 < z < 2.5$, the $\langle L_{IR,SF} \rangle$ values are systematically below the main sequence by an average factor of 0.75 (or 1.33 if taking the inverse ratio). Moving to intermediate redshifts of $0.8 < z < 1.5$ the $\langle L_{IR,SF} \rangle$ values become consistent with those of the main sequence, while at redshifts of $z < 0.8$ the $\langle L_{IR,SF} \rangle$ values move above those of the main sequence by a factor of 1.5. However, even though some of the means are not consistent within their errors, they are still consistent within the factor of 2 scatter of the main sequence (see Fig. 12a).

Following the same approach as for the full QSO sample, we estimate the expected IR luminosity of main sequence star-forming galaxies ($\langle L_{IR,MS} \rangle$) at the same redshift and stellar mass (estimated from the available M_{BH}) for our radio-luminous QSO sample, and compare to their $\langle L_{IR,SF} \rangle$. In Fig. 12(b) we show the $\langle L_{IR,SF} \rangle / \langle L_{IR,MS} \rangle$ ratio as a function of $L_{AGN,bol}$. We find that the radio-luminous QSOs have $\langle L_{IR,SF} \rangle$ values consistent with those of the main sequence within the factor of 2 scatter of the main sequence relation, which show the same redshift dependence as the full sample. Similar results were shown by Drouart et al. (2014) at $z < 2.5$, following a similar SED fitting approach, for a smaller sample of 70 powerful radio galaxies from the *Herschel* Radio Galaxy Evolution (HeRGE) sample. Additionally a number of studies have argued for radio-AGN/QSOs living in star-forming galaxies up to redshifts of ∼5 (e.g. Drouart et al. 2014; Magliocchetti et al. 2016; Rees et al. 2016) following a variety of approaches.

The relative offset between our results and the main sequence of star-forming galaxies will be dependent on the M_*–M_{BH} relation and redshift evolution assumed. We have performed the same procedure for two other cases of M_*–M_{BH} relations with and without redshift evolution. In one case we used the Kormendy & Ho (2013) relation, with no redshift evolution and assuming $M_* \approx M_{bulge}$. In the second case we used the Häring & Rix (2004) relation,
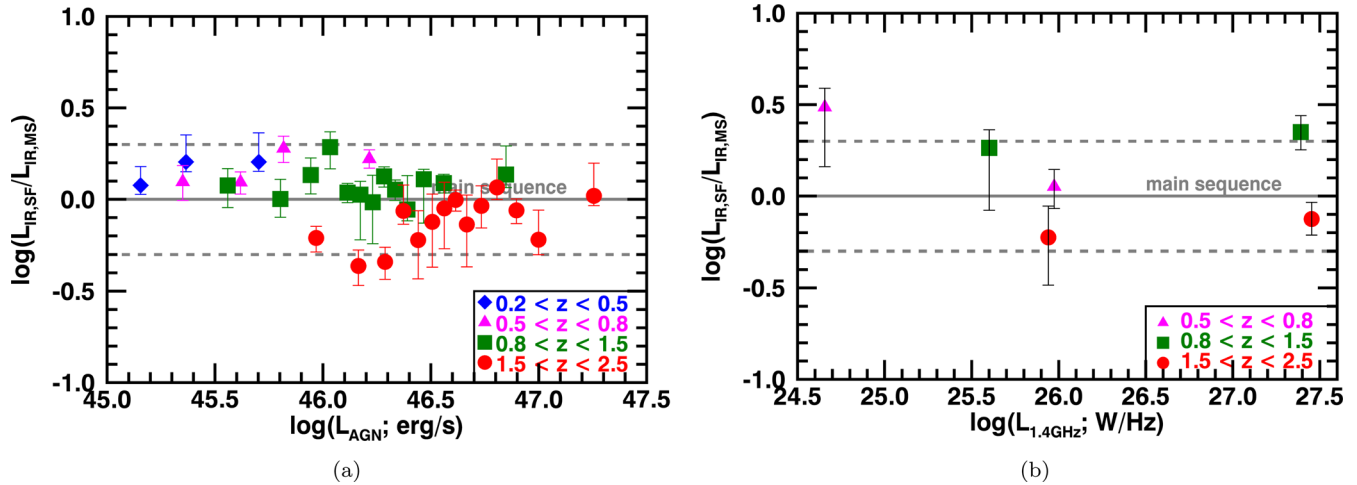
Figure 12. (a) The ratio of the $\langle L_{IR,SF} \rangle$ to $\langle L_{IR,MS} \rangle$ as a function of $L_{AGN,bol}$. The errors on the ratio are the combination of both the errors on $\langle L_{IR,SF} \rangle$ and $\langle L_{IR,MS} \rangle$. The dashed lines indicate a factor of 2 offset, characteristic of the error on the main-sequence equation. There is an apparent trend of $\langle L_{IR,SF} \rangle / \langle L_{IR,MS} \rangle$ with redshift when compared to the main sequence of star-forming galaxies, moving from having comparatively high $\langle L_{IR,SF} \rangle$ values at low redshifts ($0.2 < z < 0.5$) to consistent and comparatively low $\langle L_{IR,SF} \rangle$ values at the highest redshift range of our sample ($1.5 < z < 2.5$). (b) The ratio of the $\langle L_{IR,SF} \rangle$ of the radio-luminous QSOs over the $\langle L_{IR,MS} \rangle$ of the main sequence for galaxies of the same stellar mass and redshift, as a function of $L_{1.4\,GHz}$. We find that the $\langle L_{IR,SF} \rangle$ of radio-luminous QSOs are consistent with those of main sequence and starbursts galaxies for redshifts of $0.5 < z < 1.5$. At higher redshifts of $1.5 < z < 2.5$ the radio-luminous QSOs show lower values of $\langle L_{IR,SF} \rangle$ relative to the main-sequence galaxies, in agreement with what we see for the overall sample. We note that, for both the full sample and the radio-luminous QSO subsample, the highest redshift range ($1.5 < z < 2.5$) is affected by the uncertain systematics on deriving the stellar mass, and the choice of AGN template. Consequently, the differences in the results of the highest redshift bin and the rest of the sample should not be overinterpreted (see discussion in Section 5.2.1).

following the redshift evolution of Merloni et al. (2010). In both cases the trends of $L_{IR,MS}$ with $L_{AGN,bol}$ are similar to those seen when using the Bennert et al. (2011) relation. The $\langle L_{IR,SF} \rangle / L_{IR,MS}$ values remain within a factor of 1.25 of those estimated with the Bennert et al. (2011) relation, and remain within the factor of 2 scatter of the main sequence. Furthermore, it is also possible for QSOs in our sample to be caught in a phase of having a larger M_{BH} than that expected by the local $M_* - M_{BH}$ relation. However, for this to have a significant impact on the results presented in this section, the majority of the sources in each bin will need to systematically have overmassive BHs, by at least a factor of 2–3. By combining the work of Portinari et al. (2012), which looked into the $M_* - M_{BH}$ relation as a function of redshift for QSOs from semi analytical models (SAMs), and the redshift evolution in equation (4), we find that the M_{BH} values could be overmassive by only a factor of ~1.3. Consequently, the $\langle L_{IR,SF} \rangle$ would still remain within the factor of 2 scatter of the main sequence.

In addition to the above, we note that there is further uncertainty for the comparison to the main-sequence galaxies for our highest redshift range ($1.5 < z < 2.5$). As shown in Section 5.1.2 the highest redshift range is the one most affected by the choice of AGN template. Furthermore, for at least half the sources in this redshift range the BH masses have been estimated from the C IV line, argued to lead to overestimation of the BH mass due to observed blueshifts of the line caused by non-virial processes (see Coatman et al. 2017 and references therein). For this reason we do not strongly interpret the observed offset of the $\langle L_{IR,SF} \rangle$ to $L_{IR,MS}$ for the highest redshift range.

Overall, the $\langle L_{IR,SF} \rangle$ values of QSOs are consistent with those of main sequence star-forming galaxies within the factor of 2 scatter of the relation. Additionally, the positive trends observed in the $\langle L_{IR,SF} \rangle$ as a function of $L_{AGN,bol}$ seem to follow those expected for $\langle L_{IR,MS} \rangle$ (see Fig. 11), suggesting that the observed correlation between $\langle L_{IR,SF} \rangle$ and $L_{AGN,bol}$ is primarily driven by the stellar

masses and redshifts of the QSOs. We see no evidence for positive or negative AGN feedback as inferred from some previous studies (e.g. Kalfountzou et al. 2014; Karouzos et al. 2014).

5.2.2 The effect of AGN on the star formation of their host galaxies

The results of this study in combination to those of Stanley et al. (2015) are consistent with a scenario where AGN are on average hosted by predominately normal star-forming galaxies (see Section 5.2.1). The trends of the mean SFR with $L_{AGN,bol}$ shown in Fig. 9 can be explained by a model where AGN have a broad range of luminosities for a fixed galaxy stellar mass (Aird et al. 2013) due to a stochastic triggering mechanism of AGN and/or AGN variability on shorter time-scales than those of star formation (Hickox et al. 2014; also see section 4.3 of Stanley et al. 2015). The transition from a flat trend to a positive trend of the mean SFR with AGN luminosity seen at the highest luminosities can still be explained with the same scenario (see Fig. 11). For such high AGN luminosities, as those of our QSO sample, the range of stellar masses of the host galaxies narrows towards the more massive galaxies that will also contain more cold gas to fuel the AGN and star formation. Consequently, it is not surprising to see an increase in the SFRs of these galaxies. Indeed, in the previous section we have demonstrated that mass effects are driving the observed trends.

However, it is worth noting here that our study has concentrated on HERG-type AGN, and we do not consider the possible differences between the two excitation level types in AGN. Gürkan et al. (2015) split AGN at $z < 0.6$ into LERGs and HERGs, and found that LERGs have lower levels of star formation compared to HERGs. As HERGs and LERGs represent AGN populations with potentially different fuelling mechanisms (e.g. Hardcastle, Evans & Croston 2007; Best & Heckman 2012; Heckman & Best 2014), it is argued that they are hosted by galaxies that are at different stages of their evolution (e.g. Gürkan et al. 2015).

It is likely that any effects of the AGN on star formation are comparatively subtle, and not easily traceable when looking at the mean AGN and galaxy properties. Indeed, using a small number of sources with deep Atacama Large Millimeter/submillimeter Array (ALMA) observations, Mullaney et al. (2015) demonstrated the potential for subtle differences between the SFR *distributions* of the host galaxies of moderate luminosity AGN and main sequence star-forming galaxies. Furthermore, the flat trends of SFR with AGN luminosity have been reproduced by the EAGLE simulation (McAlpine et al. 2017), which includes AGN feedback as a crucial component of galaxy evolution (Crain et al. 2015; Schaye et al. 2015). The above results demonstrate that galaxies can show no dependence of their mean SFRs on AGN luminosity, while still being affected by AGN feedback (also see Harrison 2017).

6 CONCLUSIONS

The aim of this work has been to constrain the mean SFRs of a sample of $z = 0.2$–2.5 QSOs with AGN bolometric luminosities of $10^{45} < L_{AGN,bol} < 10^{48}$ erg s^{-1}. We investigate the mean SFRs as a function of redshift and bolometric AGN luminosity of the whole sample, and a radio-luminous subsample with $L_{1.4\,GHz} > 10^{24}$ W Hz^{-1}. We combine the five *Herschel* bands (100–500 μm) of the H-ATLAS survey to the MIR bands (12 and 22 μm) of *WISE*, and perform SED fitting to the mean fluxes of 34 $L_{AGN,bol}$–z bins of our full QSO sample and six $L_{1.4\,GHz}$–z bins of the RL-QSO subsample. We find the following.

(i) It is important to take into account of AGN contamination in the FIR when calculating the SFRs of QSOs, especially at $z > 1.5$ where the AGN can cause an overestimation of the SFR by up to a factor of 2–2.5 when derived from the flux density at observed frame 250 μm (see Section 4.1).

(ii) The mean SFRs of the optical QSOs show a positive trend with AGN luminosity (see Section 4.2). We find that this trend is dominated by BH mass and redshift dependencies on the IR luminosity due to star formation (see Section 5.2.1).

(iii) We combine the results of our optical QSO sample to lower AGN luminosity X-ray selected AGN from Stanley et al. (2015), and find that the two samples show consistent mean SFRs at overlapping AGN luminosities, for each redshift range (see Section 4.2).

(iv) Assuming that the BH and stellar mass of optical QSOs are correlated, we find that their mean SFRs are consistent to those of main-sequence galaxies within the factor of ∼2 scatter of the relation. Additionally, the weak positive trend between the mean SFR and AGN luminosity seems to follow those of the main sequence, suggesting that the trends are driven by the mass and redshift dependencies (see Section 5.2.1).

(v) The radio-luminous QSOs show consistent results to the overall optical QSO sample (see Section 4.3), and are consistent to the main sequence of star-forming galaxies within the factor of 2 scatter of the relation (see Section 5.2.1). However, at luminosities of $\langle L_{1.4\,GHz} \rangle > 10^{27}$ W Hz^{-1}, the $\langle L_{IR,SF} \rangle$ is highly uncertain due to contamination from synchrotron radiation (see Section 4.3).

Overall, our results are consistent with a scenario where X-ray and optically selected AGN are hosted on average by normal star-forming galaxies, and show no clear evidence of an increase or decrease of the SFR, on average, due to the presence of the AGN. However, this result cannot rule out a scenario where AGN are responsible for the suppression of star formation, as the time-scales for the suppression of star formation may be longer than those of luminous AGN activity (i.e. Harrison 2017). Deeper observations

are required to properly constrain the individual source properties of the AGN population. Key progress will be made by combining theoretical predictions with observational constraints on the SFR *distributions* of AGN to establish the subtle features of AGN feedback, if any.

REFERENCES

Aird J. et al., 2012, ApJ, 746, 90
Aird J. et al., 2013, ApJ, 775, 41
Alexander D. M., Hickox R. C., 2012, New Astron. Rev., 56, 93
Antonucci R., 1993, ARAA, 31, 473
Azadi M. et al., 2015, ApJ, 806, 187
Becker R. H., White R. L., Helfand D. J., 1995, ApJ, 450, 559
Bennert V. N., Auger M. W., Treu T., Woo J.-H., Malkan M. A., 2011, ApJ, 742, 107
Best P. N., Heckman T. M., 2012, MNRAS, 421, 1569
Bonfield D. G. et al., 2011, MNRAS, 416, 13
Bourne N. et al., 2016, MNRAS, 462, 1714
Bower R. G., Benson A. J., Malbon R., Helly J. C., Frenk C. S., Baugh C. M., Cole S., Lacey C. G., 2006, MNRAS, 370, 645
Bower R. G., Schaye J., Frenk C. S., Theuns T., Schaller M., Crain R. A., McAlpine S., 2017, MNRAS, 365, 32
Bruzual G., Charlot S., 2003, MNRAS, 344, 1000
Calzetti D. et al., 2010, ApJ, 714, 1256
Casey C. M., Narayanan D., Cooray A., 2014, Phys. Rep., 541, 45
Chabrier G., 2003, PASP, 115, 763
Coatman L., Hewett P. C., Banerji M., Richards G. T., Hennawi J. F., Prochaska J. X., 2017, MNRAS, 465, 2120
Crain R. A. et al., 2015, MNRAS, 450, 1937
Del Moro A. et al., 2013, A&A, 549, A59
Delvecchio I. et al., 2014, MNRAS, 439, 2736
Di Matteo T., Springel V., Hernquist L., 2005, Nature, 433, 604
Domínguez Sánchez H. et al., 2014, MNRAS, 441, 2
Drouart G. et al., 2014, A&A, 566, A53
Drouart G., Rocca-Volmerange B., De Breuck C., Fioc M., Lehnert M., Seymour N., Stern D., Vernet J., 2016, A&A, 593, A109
Eales S. et al., 2010, PASP, 122, 499
Elbaz D. et al., 2007, A&A, 468, 33
Elbaz D. et al., 2011, A&A, 533, A119
Fabian A. C., 2012, ARA&A, 50, 455

Feigelson E. D., Nelson P. I., 1985, ApJ, 293, 192
Genel S. et al., 2014, MNRAS, 445, 175
Gürkan G. et al., 2015, MNRAS, 452, 3776
Hardcastle M. J., Evans D. A., Croston J. H., 2007, MNRAS, 376, 1849
Hardcastle M. J. et al., 2013, MNRAS, 429, 2407
Häring N., Rix H.-W., 2004, ApJ, 604, L89
Harris K. et al., 2016, MNRAS, 457, 4179
Harrison C. M., 2017, Nat. Astron., 1, 0165
Harrison C. M. et al., 2012, ApJ, 760, L15
Heckman T. M., Best P. N., 2014, ARA&A, 52, 589
Hickox R. C., Mullaney J. R., Alexander D. M., Chen C.-T. J., Civano F. M., Goulding A. D., Hainline K. N., 2014, ApJ, 782, 9
Kalfountzou E. et al., 2014, MNRAS, 442, 1181
Karouzos M. et al., 2014, ApJ, 784, 137
Kellermann K. I., Sramek R., Schmidt M., Shaffer D. B., Green R., 1989, AJ, 98, 1195
Kennicutt R. C., Jr, 1998, ARA&A, 36, 189
Kormendy J., Ho L. C., 2013, ARA&A, 51, 511
Lani C., Netzer H., Lutz D., 2017, MNRAS, 471, 59
Lanzuisi G. et al., 2017, A&A, 602, A123
Liddle A. R., 2004, MNRAS, 351, L49
Lutz D., 2014, ARA&A, 52, 373
Lyu J., Rieke G. H., 2017, ApJ, 841, 76
McAlpine K., Jarvis M. J., Bonfield D. G., 2013, MNRAS, 436, 1084
McAlpine S., Bower R. G., Harrison C. M., Crain R. A., Schaller M., Schaye J., Theuns T., 2017, MNRAS, 468, 3395
Magliocchetti M. et al., 2014, MNRAS, 442, 682
Magliocchetti M., Lutz D., Santini P., Salvato M., Popesso P., Berta S., Pozzi F., 2016, MNRAS, 456, 431
Magnelli B. et al., 2014, A&A, 561, A86
Merloni A. et al., 2010, ApJ, 708, 137
Mor R., Netzer H., 2012, MNRAS, 420, 526
Mullaney J. R., Alexander D. M., Goulding A. D., Hickox R. C., 2011, MNRAS, 414, 1082
Mullaney J. R. et al., 2012, MNRAS, 419, 95
Mullaney J. R. et al., 2015, MNRAS, 453, L83
Netzer H. et al., 2007, ApJ, 666, 806
Netzer H., Lani C., Nordon R., Trakhtenbrot B., Lira P., Shemmer O., 2016, ApJ, 819, 123
Noeske K. G. et al., 2007, ApJ, 660, L43
Page M. J. et al., 2012, Nature, 485, 213
Pannella M. et al., 2015, ApJ, 807, 141
Pilbratt G. L. et al., 2010, A&A, 518, L1
Pineau F.-X., Motch C., Carrera F., Della Ceca R., Derrière S., Michel L., Schwope A., Watson M. G., 2011, A&A, 527, A126
Pitchford L. K. et al., 2016, MNRAS, 462, 4067

Podigachoski P., Rocca-Volmerange B., Barthel P., Drouart G., Fioc M., 2016, MNRAS, 462, 4183
Portinari L., Kotilainen J., Falomo R., Decarli R., 2012, MNRAS, 420, 732
Rees G. A. et al., 2016, MNRAS, 455, 2731
Richards G. T. et al., 2006, ApJS, 166, 470
Rosario D. J. et al., 2012, A&A, 545, A45
Rosario D. J. et al., 2013, A&A, 560, A72
Rosario D. J., Mendel J. T., Ellison S. L., Lutz D., Trump J. R., 2016, MNRAS, 457, 2703
Schaye J. et al., 2015, MNRAS, 446, 521
Schneider D. P. et al., 2010, AJ, 139, 2360
Schneider R., Bianchi S., Valiante R., Risaliti G., Salvadori S., 2015, A&A, 579, A60
Schreiber C. et al., 2015, A&A, 575, A74
Schwarz G., 1978, Ann. Stat., 6, 461
Serjeant S. et al., 2010, A&A, 518, L7
Seymour N. et al., 2011, MNRAS, 413, 1777
Shen Y. et al., 2011, ApJS, 194, 45
Silva L., Granato G. L., Bressan A., Danese L., 1998, ApJ, 509, 103
Stanley F., Harrison C. M., Alexander D. M., Swinbank A. M., Aird J. A., Del Moro A., Hickox R. C., Mullaney J. R., 2015, MNRAS, 453, 591
Stern D. et al., 2012, ApJ, 753, 30
Symeonidis M., Giblin B. M., Page M. J., Pearson C., Bendo G., Seymour N., Oliver S. J., 2016, MNRAS, 459, 257
Thacker R. J., MacMackin C., Wurster J., Hobbs A., 2014, MNRAS, 443, 1125
Valiante E. et al., 2016, MNRAS, 462, 3146
Volonteri M., Capelo P. R., Netzer H., Bellovary J., Dotti M., Governato F., 2015, MNRAS, 449, 1470
Wang L. et al., 2015, MNRAS, 449, 4476
Whitaker K. E., van Dokkum P. G., Brammer G., Franx M., 2012, ApJ, 754, L29
White M. et al., 2012, MNRAS, 424, 933
Wright E. L. et al., 2010, AJ, 140, 1868

APPENDIX A: SED FITS FOR ALL BINS

In this section we present the best-fitting SEDs for all bins in our sample. In Fig. A1 we show the best fits of each bin for our full QSO sample, with IDs that correspond to those of Table 1. In Fig. A2 we show the best fits for our radio-luminous subsample, with IDs that correspond to those of Table 2.
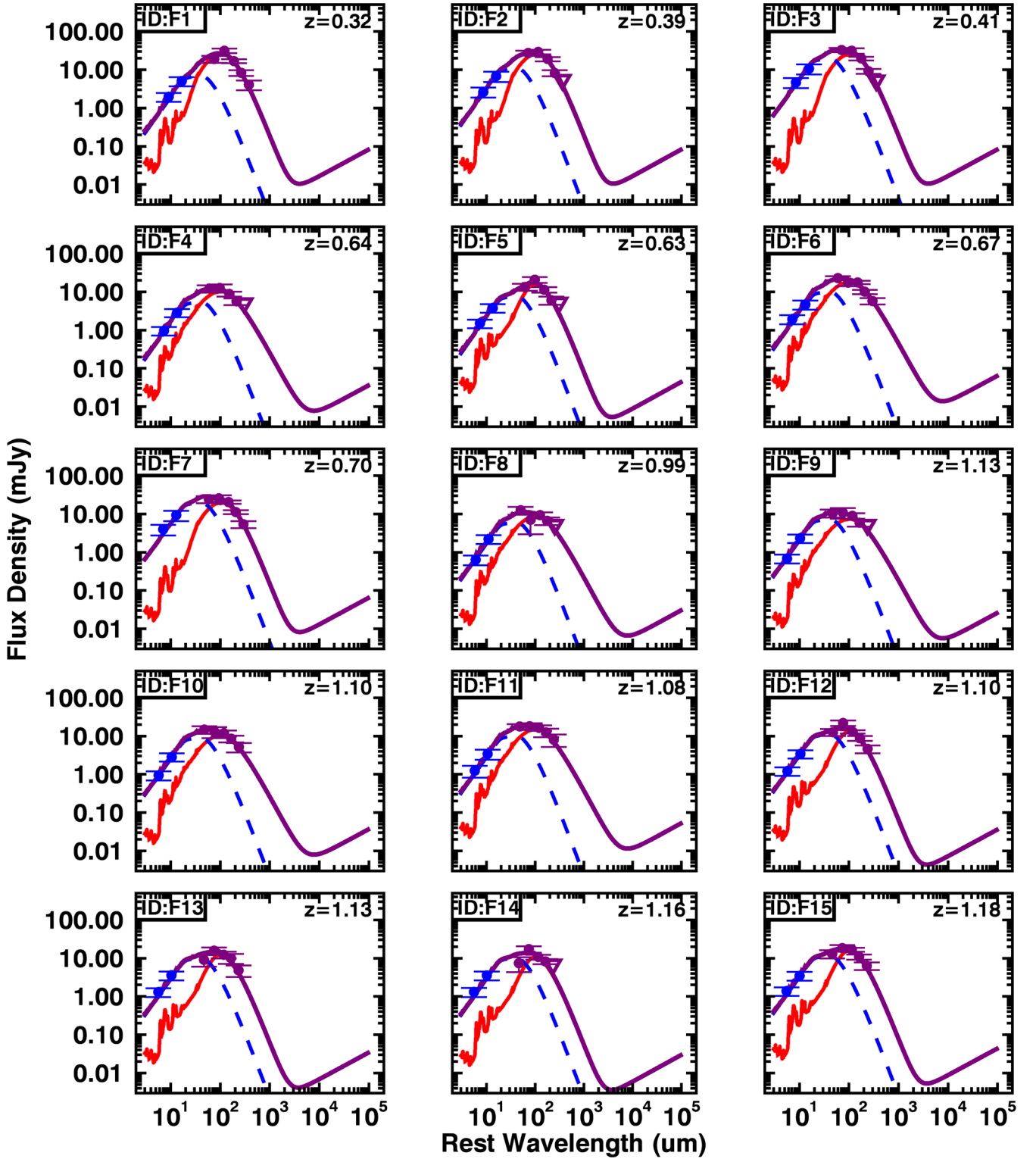
Figure A1. The best-fitting SEDs for all the z–$L_{AGN,bol}$ bins of the QSO sample. The data points correspond to the mean photometry of each bin and the downwards pointing triangles correspond to the upper limits. The blue dashed curve is the AGN component of the SED, the red solid curve is the star-forming component and the purple solid curve corresponds to the total IR SED. The ID name corresponds to that of Table 1 for direct reference, and the redshift corresponds to the mean redshift of the sources in the z–$L_{AGN,bol}$ bin.
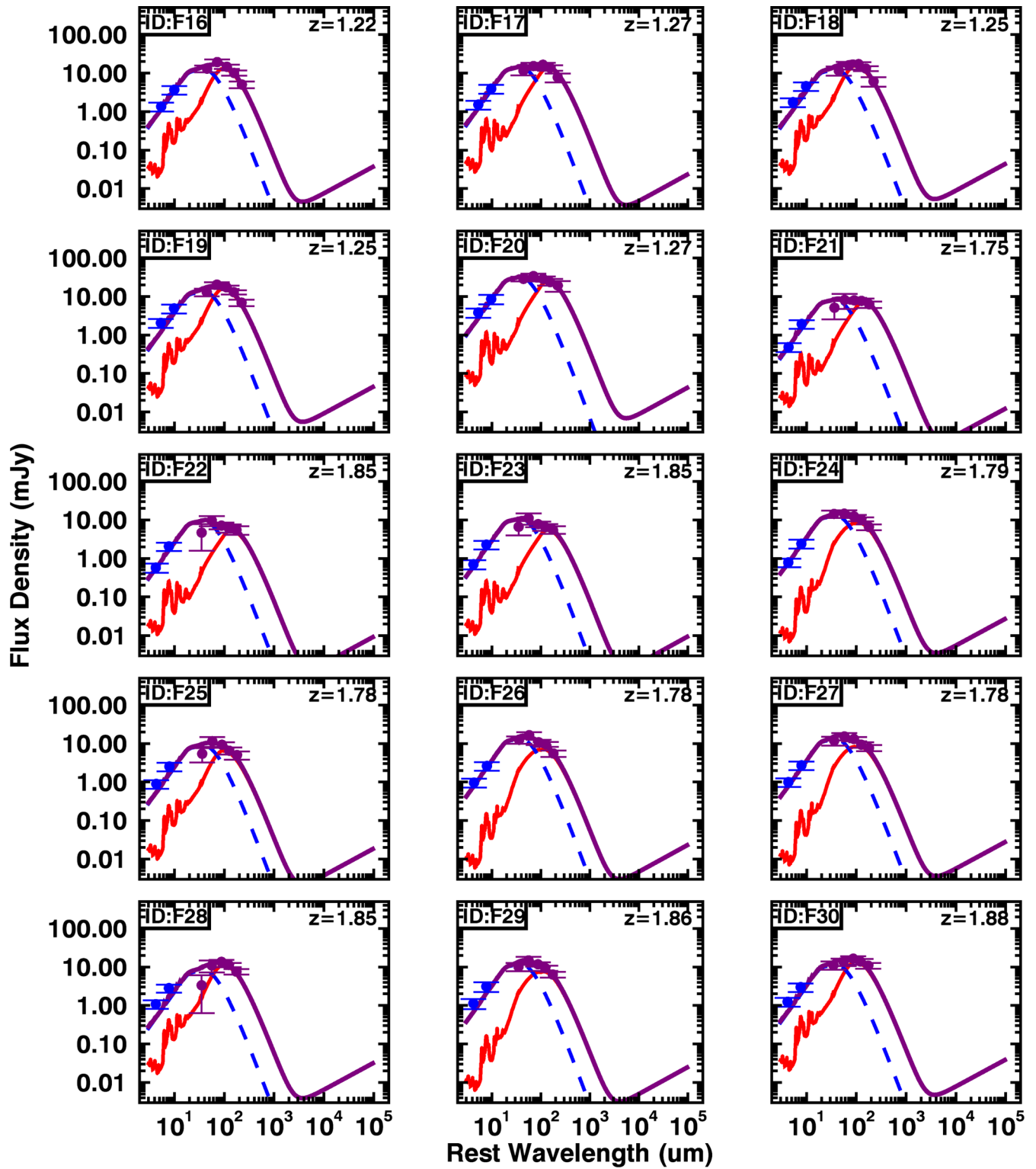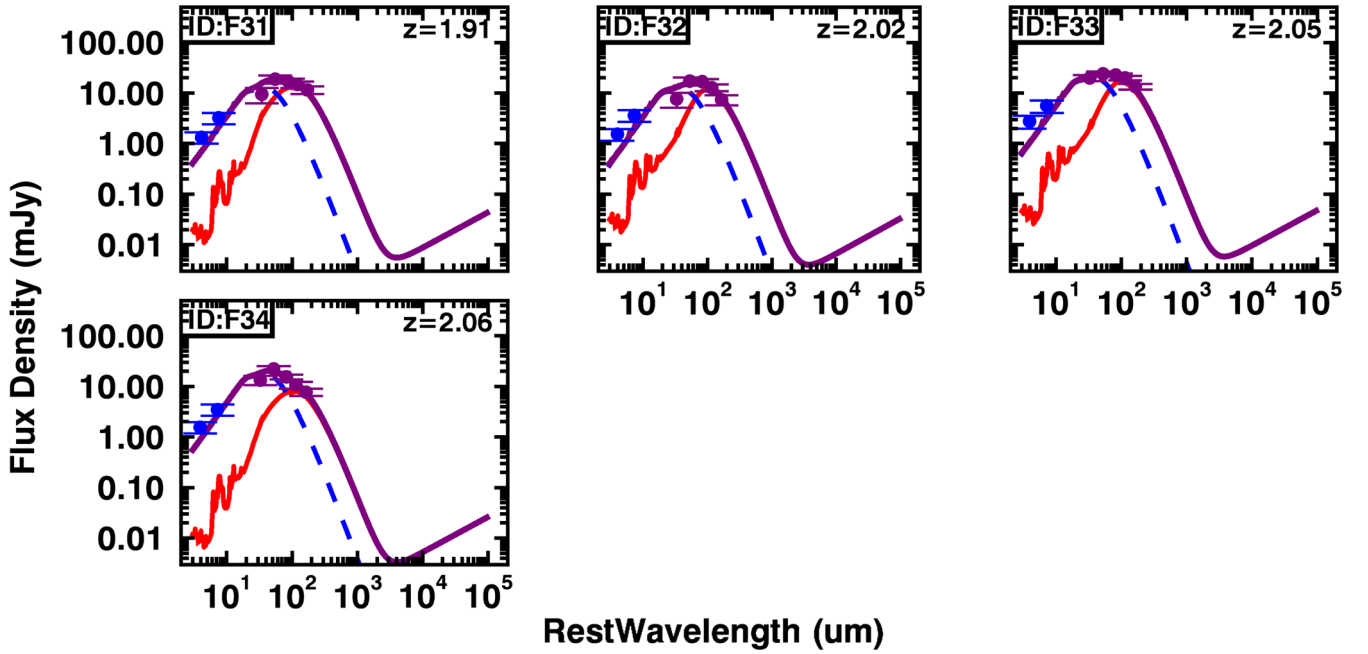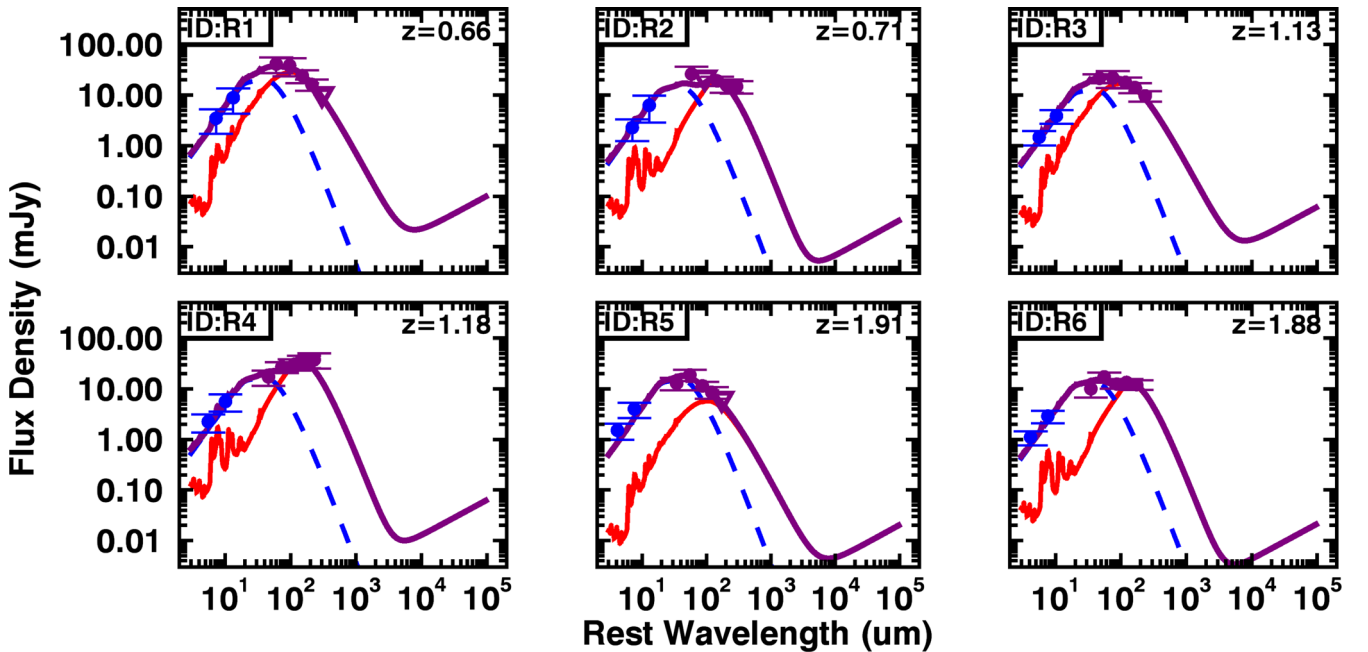
Figure A1 *continued*

Figure A1 *continued*

Figure A2. The best-fitting SEDs for all the z–$L_{1.4\ GHz}$ bins of the RL–QSO sample. The data points correspond to the mean photometry of each bin and the downwards pointing triangles correspond to the upper limits. The blue dashed curve is the AGN component of the SED, the red solid curve is the star-forming component and the purple solid curve corresponds to the total IR SED. The IDs correspond to those of Table 2 for direct reference, and the redshift corresponds to the mean redshift of the sources in the z–$L_{1.4\ GHz}$ bin.

APPENDIX B: THE RADIAL LIGHT PROFILE OF SPIRE STACKED SOURCES

An additional cause for uncertainty in the SPIRE stacked flux density estimates is the possible boosting due to nearby sources. QSOs are well known to be clustered (e.g. White et al. 2012 and references therein), and in Wang et al. (2015) it was found that due to the clustering of other dusty star-forming galaxies around optical QSOs there is a ∼8–13 per cent contamination to the 250–500 μm flux density, respectively. To take this possible source of contamination into account, we measure the average flux density in annuli, and fit the flux density as a function of radius from the centre to a radius of ∼150 arcsec. We use the SPIRE PSF (provided by H-ATLAS) convolved with itself, which corresponds to the images we
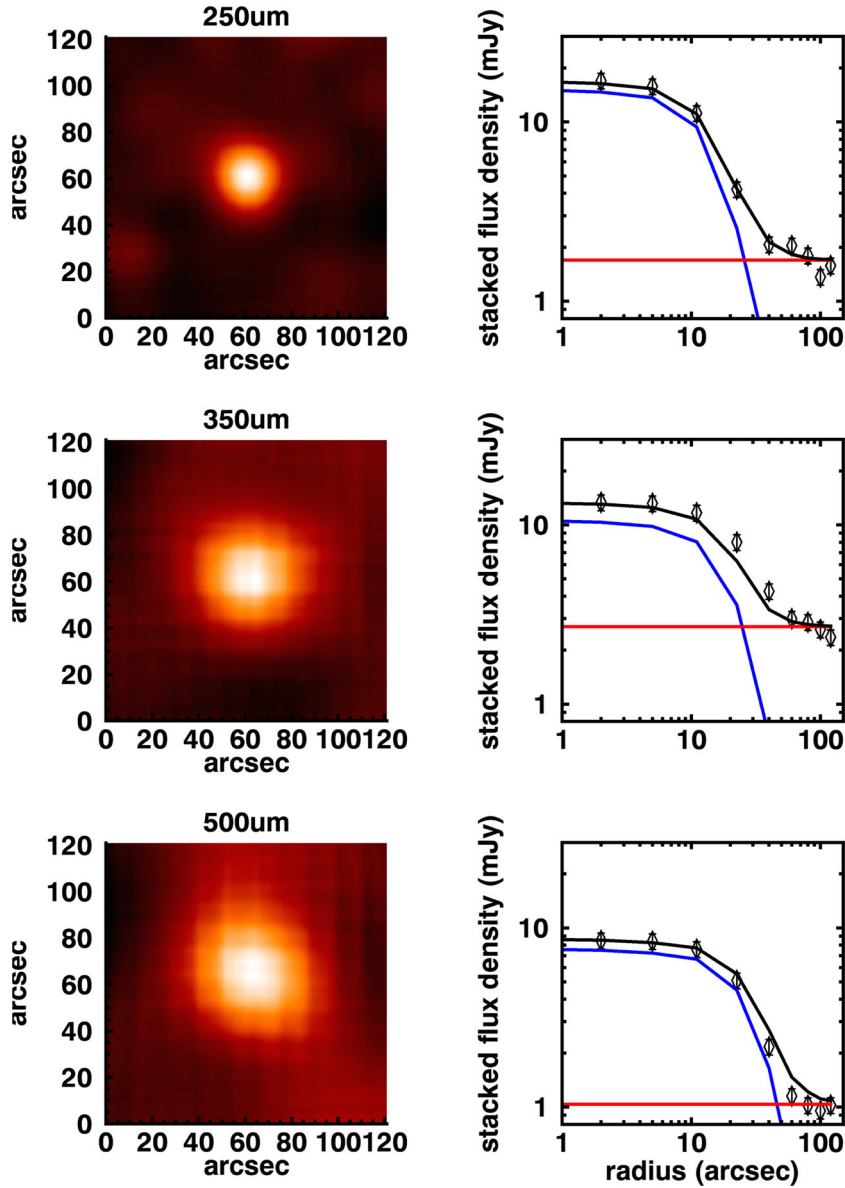
Figure B1. Examples of our radial light profile analysis for the three SPIRE bands. In the left-hand panels are the stacked images in 250, 350 and 500 μm. In the right-hand panel we show examples of the radial light profile of the stacked image used to estimate the contamination from bright neighbouring sources. The light profile is fitted with the convolved PSF (blue) for each band, respectively, and a constant flux density level fitted to the high-end tail for the estimation of the contamination factor to the stacked flux density (red).

are using, and a constant flux density level that is free to vary (see last panel in Fig. B1).[6] The factor of contamination calculated for each bin shows no dependency on redshift and AGN luminosity, and has a median of ~11 per cent at 250 μm, 24 per cent at 350 μm and 14 per cent at 500 μm. However, the absolute values of the contamination factor are equivalent to the offset that we see in the random stack distribution, which we have used when correcting the stacked flux densities. Consequently, the contamination measured here is still only constraining the confusion background of our fits, and there may be an additional contamination factor due to clustering that we cannot constrain here.

---

[6] To define the amount of contamination from nearby sources, we originally used a combination of the convolved PSF and a power law of fixed slope. Because of the quality of the data we cannot place a strong constraint on the slope of the power law. For this reason we fitted with different fixed power-law slopes and chose to use the one with the lowest χ^2 values, which corresponds to a slope of zero (i.e. a constant flux density level).

This paper has been typeset from a TEX/LATEX file prepared by the author.